Studia Quaternaria, vol. 43 (2026): 33–54
DOI: 10.24425/sq.2026.158730

REMOTE SENSING STUDY OF 30-YEAR SHORELINE MOVEMENT ON THE ROSETTA PROMONTORY RELATED TO THE SPATIAL VARIATIONS IN SEDIMENT GRAIN SIZE AND HEAVY MINERAL CONCENTRATION

Eman A. Elsherif[1,2*], Amani Badawi[2], Jakub Ciążela[1], Tarek Abdelkader[3]

[1] *Institute of Geological Sciences, Polish Academy of Sciences, Podwale Str. 75, 50-449 Wrocław, Poland; e-mails: EAE emanadelelsherif@yahoo.com, JC j.ciazela@twarda.pan.pl*
[2] *National Institute of Oceanography and Fisheries (NIOF), Egypt; e-mail: AB amani_badawi@yahoo.com*
[3] *Geology Department, Faculty of Science, Tanta University, Egypt; e-mail: TA tarek.abdelkader@science.tanta.edu.eg*
** corresponding author*

Abstract:
The Rosetta promontory, situated at the western mouth of the Nile Delta, represents one of the most erosion-vulnerable sectors of the Egyptian Mediterranean coastline. This study presents an integrated multi-temporal shoreline change analysis, employing satellite-derived DSAS mapping over 1999–2019 and 1999–2015 alongside grain-size and heavy-mineral analyses of shoreline sediments. Shoreline change analysis of 1999–2019 revealed a dominantly erosional regime, with a mean shoreline change rate of -3.65 m/year and a mean erosion rate of 7.92 m/year, affecting 70% of the total coastline. An extreme erosion rate of 32.51 m/year was recorded downdrift of the fifth eastern groyne, reflecting groyne-field-induced sediment transport discontinuity. Without management intervention, a mean coastline recession of 108 m and net land loss of 2.24 km² are projected by 2030. Heavy mineral concentrations ranged from 0.71 to 23.14 wt.% (mean 10.21 wt.%), with the majority of locations exceeding the 2 wt.% economic viability threshold. Shoreline change rates showed weak correlation with heavy mineral concentration (R = -0.37) and negligible correlation with mean grain size (R = 0.15), both variables substantially modified by anthropogenic coastal infrastructure. These findings highlight the urgent need for integrated coastal management strategies to mitigate accelerating land loss along this vulnerable deltaic coastline.

Key words: Shoreline Change, Shoreline Forecast; Nile Delta; Rosetta Promontory; Heavy Mineral; DSAS; Coastal Erosion; Longshore Sediment Transport; Coastal management.

Manuscript received 24 March 2026, accepted 11 July 2026

INTRODUCTION

During the last century, the Nile Delta coast has faced geomorphological changes due to the combined effects of a series of natural processes and excessive anthropogenic uses (Frihy *et al*., 1991; Frihy and Komar, 1993; Frihy and Dewidar, 2003; Frihy *et al*., 2008; El Banna and Frihy, 2009; Iskander, 2010; El-Asmar and Hereher, 2010; Ghoniem *et al*., 2015). The Nile River sediments discharged into the Mediterranean Sea through its branches have governed the development and dynamics of the Nile Delta coast and associated deposits along the Mediterranean coast since the Pleistocene to Recent (Hilmy, 1951; Stanley, 1988). Following sediment delivery, hydrodynamic processes regularly modified the Nile Delta Coast's morphology by inducing longshore sedimentation patterns of erosion, accretion, and sediment transport.

Climatological risks, such as global warming and its associated impacts, such as seawater intrusion, accelerating sea level rise, and storm surges, threaten low-lying and densely populated areas of the coastal areas near the estuaries (Frihy and Khafagy, 1991; Becker and Sultan, 2009).

If the sea level rises by 100 cm above its current level, about 31% of the Nile Delta will be inundated (Hereher, 2010). This will be accompanied by the relocation of millions of people southward to the present shoreline, contamination of water resources, and loss of fertile agricultural land. The most pessimistic scenario involves the coupling of sea-level rise with delta subsidence, which is estimated at 4.5 mm/year in the northern part of the Nile Delta. This situation will trigger the inundation threat (Marriner *et al*., 2012). In the Rosetta area, a relative SLR of 4.9 mm/year has been attributed to land subsidence due to natural compaction and dewatering of Holocene deltaic sediments (Frihy *et al*., 2010). As a result of relative sea-level rise and land subsidence, the Rosetta promontory has a much higher coastal submergence rate of 5.4 mm/year (Stanley and Corwin, 2013). Added to these natural threats, tectonics could contribute to coastal subsidence.

The Nile Delta regime has changed from a zone of accumulation to one of depletion, primarily due to the construction of seven barrages along the Nile from Aswan to the lower Delta, the Aswan Low Dam in 1902, and the Aswan High Dam (AHD) in 1964. The construction of barrages and dams significantly controlled the magnitude of the river's peak discharge and has virtually stopped sediment delivery from reaching the coast. Since these structures were built, approximately 98% of the river's estimated annual sediment load, which is around 120–125 million tons yr^{-1}, has been trapped (Shalash, 1982; Inman and Jenkins, 1984).

Since that time, rapid erosion rates affected the Nile Delta, particularly at the terminus of the Rosetta and Damietta branches. Average rates of shoreline retreat, about 15 m per year, were encountered at the Rosetta branch, and the coastline of Rosetta promontory underwent a mean retreat of 137.4 m/year in 1991 (White and El-Asmar, 1999; Frihy *et al*., 2003; Frihy and Lawrence, 2004; Ghoneim, 2009; Ghoneim *et al*., 2015; Hereher, 2011). The eastern and western sides of the Rosetta promontory experienced shoreline losses of 4.4 and 5.8 km, respectively, between 1900 and 1991 (UNESCO/UNDP, 1978; Fanos *et al*., 1995).

To reduce rapid erosion rates, coastal protection measures were initiated in 1989, during which two 5 km-long seawalls were constructed to the west and east of Rosetta mouth between 1989 and 1991. Additionally, between 2003 and 2005, protection works continued, with the installation of 14 groynes (nine west and five east of the Rosetta branch mouth) aimed at mitigating erosion along the leeward side of both seawalls (Fig. 1). However, the coastal areas downdrift of both seawalls revealed a turn from accretion-dominated areas (3–5 m/year) to erosion-dominated areas where some eastern and western shoreline sides experienced 30.8 m/year and 20 m/year of erosion, respectively (Ghoneim *et al*., 2015). The downdrift coast is situated east of the massive coastal structures and experienced a local erosion of 25 m/year (Frihy, 2017).

However, the human efforts have mitigated rapid erosion rates by retaining sand beaches and halting the recession along the tip of the promontory, which lost 10.8 km^2, prior to coastal protection, they failed to halt coastal loss while altering the shoreline morphology along the sides of the promontory and obstructing the natural equilibrium between the sources of beach sediments and the littoral drift system (Ghoneim *et al*., 2015). Lately, the eastern coast has seen increased industrial activities due to the construction of Ghalioun fish farm, an industrial fishery city. Ghalioun fish farm is one of the largest fish projects inaugurated in 2017 in the Berket Ghalioun area. Furthermore, the coastal area is heavily exploited for mining and processing operations of the Egyptian Black Sand along the Egyptian North Coast.

Such pressures threaten the coastal ecosystem, causing substantial damage to the coastal resources. These pressures are mainly visible both near the coastal cities and at the river mouths. Thus, coastal zone monitoring is vital to bring efficient and effective solutions to preserve natural environmental resources. Shoreline position is one of the principal indicators of coastal change, and its monitoring is fundamental. Shorelines are highly dynamic geomorphic systems that exhibit changes in both space and time, driven by complex and interrelated factors. Analysing shoreline variability and erosion-accretion trends is a significant concern for a wide range of investigations (Douglas and Crowell, 2000). The most important aspect of managing coastal areas is identifying the location of the shoreline, beach width and volume and quantifying historical rates of shoreline change (Dolan *et al*., 1991; Komar, 1998; Moore, 2000). The coastal processes, such as erosion/accretion and their cumulative effects on the shoreline and human impacts in the study area, could be analysed effectively using Remote Sensing and GIS techniques. This approach has many advantages, including the extensive spatial and spectral coverage of satellite images, the temporal resolution of satellite data, the digital format of imagery, the long temporal coverage of satellite archives (Dolan *et al*., 1983) and continuous monitoring of shorelines (Kevin and El Asmar, 1999).

The Nile Delta coastline is an economically valuable area which sustains concentrations of high-grade heavy minerals. However, the distribution and concentration of heavy minerals in sediments depend mainly on the mineralogical content of the sands from which they are derived, the geomorphological features of the area, the characteristics of mineral grains, and wind strength and direction (Woolsey *et al*., 1975). There was a general consistency (modest correlation) between the seabed level changes and the distribution pattern of heavy mineral concentration along the Nile Delta Coast (Frihy and Komar, 1991, 1993; Frihy and Dewidar, 2003). The interchange between erosion and accretion processes led not only to variations in the concentration of heavy minerals in the beach sands but additionally in the mineralogical content (Frihy and Komar, 1991; Frihy and Lotfy, 1994). The highest heavy mineral concentrations mainly correspond with erosion areas where they accumulate and can be exploited. The lowest concentrations of heavy minerals coincide with accretion areas, where grains of low density preferentially accumulate. A transitional zone between eroded and accreted areas may occur with an intermediate mineral composition,

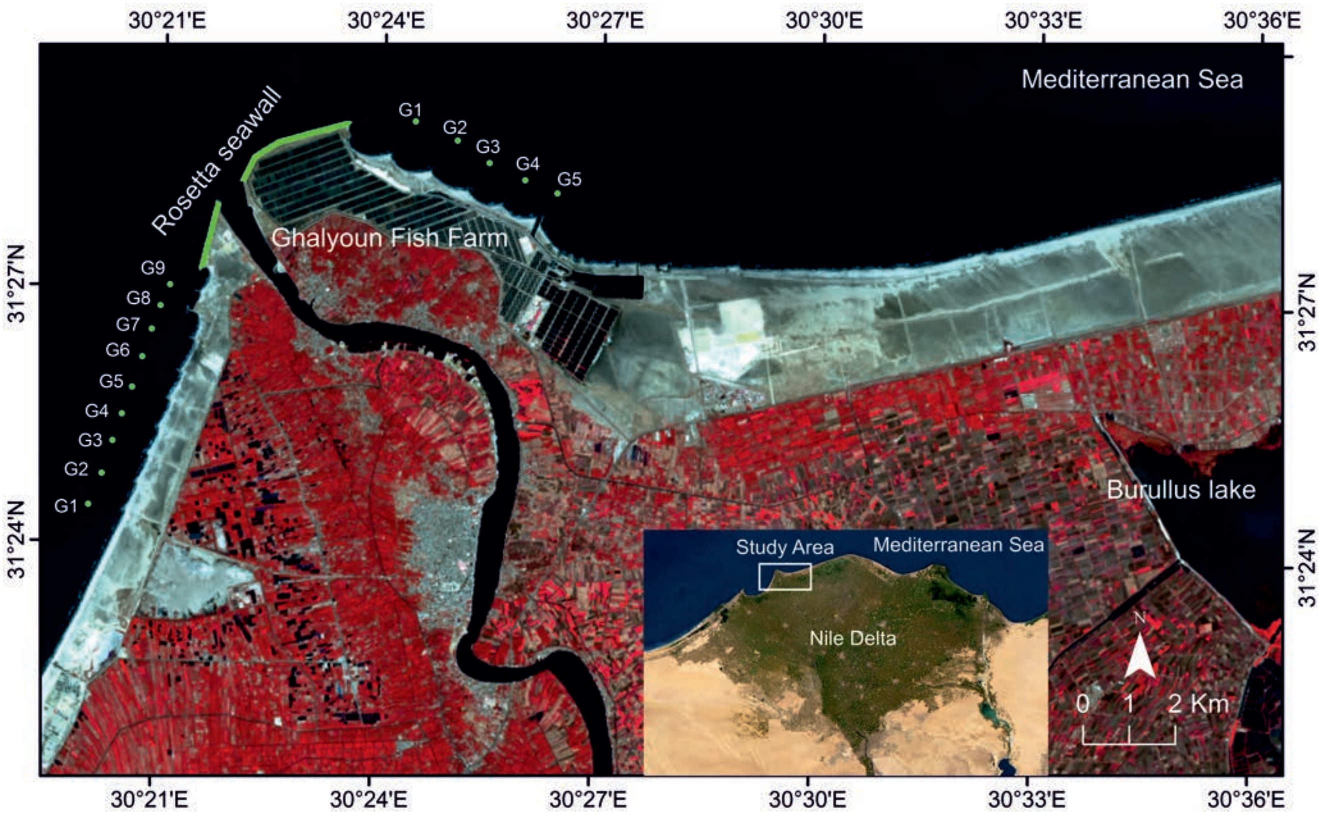

Fig. 1. Location of the study area at the Rosetta promontory, northwestern Nile Delta coast. Landsat-8 false-colour composite (bands 5, 4, and 3) showing coastal protection structures and successive groynes (green dots) on both sides of the Rosetta estuary.

which signifies a shift in the sediment regime from erosion to accretion or vice versa (Frihy and Lotfy, 1994).

The integration of satellite-derived shoreline change analysis with conventional grain-size and heavy-mineral analysis in the present study is motivated by a dual scientific rationale. Shoreline change analysis alone quantifies the spatial and temporal patterns of coastal erosion and accretion but provides no insight into the sedimentological consequences of these processes or the nature of the material being mobilised and redistributed within the littoral system. Conversely, sediment textural and mineralogical analyses characterise the composition and sorting of beach sediments but cannot, in isolation, resolve the dynamic processes driving their spatial distribution. By combining these two approaches, the present study exploits the well-established relationship among longshore sediment transport, selective hydrodynamic sorting, and the resulting spatial variability in heavy mineral concentration along wave-dominated deltaic coastlines (Frihy and Komar, 1993; Frihy and Dewidar, 2003). Erosional zones, where preferential removal of lighter quartz fractions occurs, are expected to yield residual sediments enriched in dense heavy mineral phases. Conversely, accretional zones receiving mixed sediment inputs are expected to exhibit lower heavy mineral grades. This coupled approach, therefore, allows shoreline change dynamics to be interpreted through an independent sedimentological lens, providing a more robust and process-informed understanding of littoral system behaviour. The Rosetta coastline is recognised for its valuable beach placer deposits of heavy minerals. Therefore, understanding the spatial variation between erosion-accretion patterns and concentration of heavy minerals is crucial. This knowledge directly impacts the assessment of deposit viability and the sustainable management of coastal mineral resources.

Despite the growing body of literature on Nile Delta coastal dynamics, a comprehensive updated assessment of shoreline change along the Rosetta promontory and its relationship to sediment mineralogical and textural characteristics remains lacking. To address this gap, the present study quantifies historical rates of shoreline change along the coasts surrounding the Rosetta promontory over the periods 1999–2019 and 1999–2015, and forecasts the shoreline position for 2030 based on these rates. Building on this morphodynamic foundation, the study further characterises the spatial distribution of mineralogical variability in relation to the coastal geomorphology of Rosetta. Additionally, it correlates the documented erosion and accretion patterns during 1999–2015 with heavy-mineral concentration and mean grain size of shoreline sediments. This integrated approach provides a coupled morphodynamic and sedimentological framework for understanding the response of this vulnerable deltaic coastline to both natural forcing and anthropogenic intervention, with direct implications for coastal management and shoreline stabilisation strategies in the region.

REGIONAL SETTING

The study area is situated in the north-west of the Nile delta coastline, and the westward and eastward coastlines of Rosetta Promontory are chosen for the study area (Fig. 1). The onshore western side covers the Altabiya-Rosetta area, west of the Rosetta distributary mouth, and is about 10 km long. The onshore eastern side extends along 22 km, while the most eastern stretch is considered the western sector of the sand bar separating the Burullus Lake from the Mediterranean Sea.

The coastline eastward and westward of the Rosetta promontory is nearly flat and very gently dipping (near horizontal) to the north (Nafaa and Frihy, 1993). The beach face slope near Rosetta mouth is near zero and steepens to about 15° at a distance of 20 km east of the mouth (Wassef, 1973). The coastal geomorphology of the study area comprises: the river mouth, the shoreline, and the backshore plains. The beach sediment consists of loose quartz sand mixed with variable concentrations of heavy minerals and shell fragments controlled by large-scale patterns of sand movement and sorting. The grain size of the beach sediments eastward and westward of the Rosetta promontory was surveyed, covering the beach face area to the backshore, and showed a predominance of well-sorted fine sand sediment (approximately 79% of the sand content; Elsherif *et al.*, 2020).

The Nile Delta is considered a river-dominated sedimentation type delta that is additionally influenced by waves and coastal currents (Manohar, 1976; 1981; Coleman *et al.*, 1981; Smith and Abdel-Kader, 1988). However, the Rosetta promontory exhibits varying coastal dynamics due to its unique shoreline orientation, which modifies the influence of waves and currents against the prevailing conditions along the rest of the delta coast. The coastline east of the Rosetta promontory is exposed to prevailing waves from the N, NNW, NW, WNW, NNE and NE directions, generating a southeasterly longshore current which transports sediments eroded from the promontory tip eastward and deposits them in the southeast saddle areas (Frihy *et al.*, 2003). In contrast, the coastline west of the Rosetta promontory is influenced by a westerly longshore current driven by N and NW wave directions, which transports sediments eroded from the southwestern flank of the promontory tip westward along Abu Quir Bay (Fig. 2). Wave action along

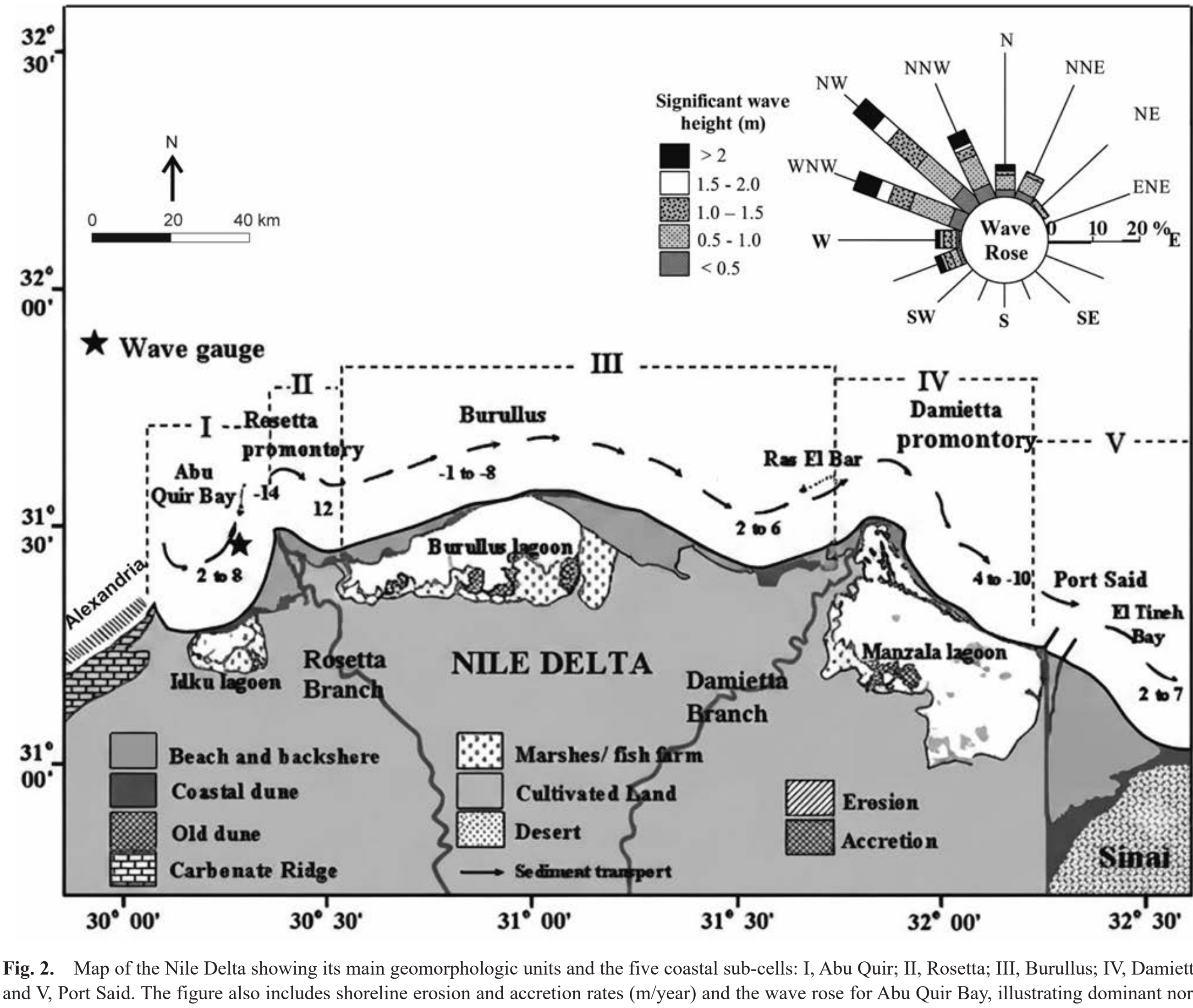

Fig. 2. Map of the Nile Delta showing its main geomorphologic units and the five coastal sub-cells: I, Abu Quir; II, Rosetta; III, Burullus; IV, Damietta; and V, Port Said. The figure also includes shoreline erosion and accretion rates (m/year) and the wave rose for Abu Quir Bay, illustrating dominant north and northwest wave directions with significant northeast reversals (modified from Frihy *et al.*, 2003).

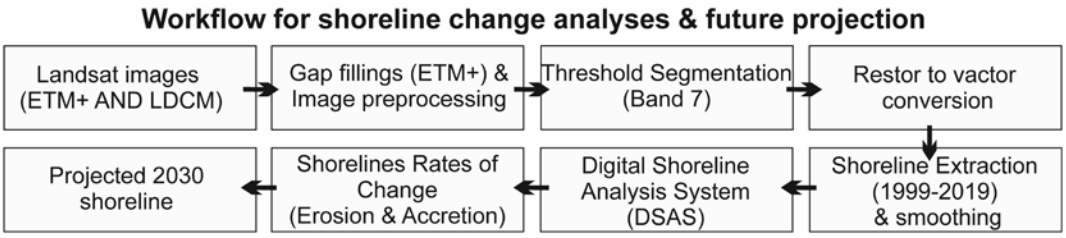

Fig. 3. Flowchart of the methodology used in this study.

the study coastline is seasonally variable. During winter and spring, the coast experiences high-energy waves, with significant heights of 2–3 m, predominantly coming from the NNW or WNW. These conditions contrast markedly with the calmer summer months, during which wave heights decrease substantially to 40–75 cm, while maintaining the same prevailing NNW and WNW approach directions (Manohar, 1976; El Wany *et al*., 1988).

On average, the wave height and period for the Rosetta promontory are 1.2 m and 5.6 s, respectively (Frihy *et al*., 2003). The wave breaker height is significant in determining the quantity of sand in motion, and the wave breaker direction is important in determining the direction and rate of longshore movement. Wave-induced longshore currents are the primary coastal processes which cause morphologic changes along the Rosetta promontory. The role of tides in coastal processes is almost insignificant and semidiurnal, with an average tidal difference along the Nile Delta between normal high-water line (NHWL) and normal low-water line (NLWL) of the order of 25 to 30 cm (Manohar, 1981).

Analyses of seabed level and shoreline changes in combination with textural and mineralogical analyses were studied along the Nile Delta and featured a series of discrete sedimentation compartments that were differentiated into four littoral subcells within the regional littoral zone (Frihy *et al*., 1991; Frihy and Lotfy, 1997). These four littoral sub-cells along the delta itself are identified as Abu Quir, Rosetta, Burullus, Damietta and Port Said by Orlova and Zenkovitch (1974), and Frihy *et al*. (1991) (Fig. 2). Each cell represents a complete cycle of erosion, transport and accretion (Inman and Brush, 1973). The study area comprised the western and eastern parts adjacent to the Rosetta mouth, which were parts of Abu Quir and Rosetta subcells, respectively. The easternmost coastal area of the study area was identified as the erosion zone of the Burullus subcell. The transport pattern within the study area showed a divergence pattern influenced by the coastal geomorphology. Specifically, the Abu Quir subcell directed littoral sediment transport westward, while the Rosetta subcell directed it eastward. This movement was induced by wave and longshore currents, which created transport paths along the coast.

Table 1. Satellite sensors adopted in this study.

Acquired date	Sensor Type	Spatial resolution (m)	Spectral resolution (no. of bands)
29/09/1999	Landsat ETM+	30	8
13/07/2000	Landsat ETM+	30	8
29/05/2001	Landsat ETM+	30	8
19/07/2002	Landsat ETM+	30	8
03/05/2003	Landsat ETM+	30	8
09/08/2004	Landsat ETM+(SLC-off)	30	8
13/09/2005	Landsat ETM+ (SLC-off)	30	8
12/6/2006	Landsat ETM+ (SLC-off)	30	8
17/07/2007	Landsat ETM+ (SLC-off)	30	8
17/06/2008	Landsat ETM+ (SLC-off)	30	8
06/05/2010	Landsat ETM+ (SLC-off)	30	8
28/07/2011	Landsat ETM+ (SLC-off)	30	8
14/07/2012	Landsat ETM+ (SLC-off)	30	8
25/07/2013	Landsat 8 (LDCM)	30	11
28/07/2014	Landsat 8 (LDCM)	30	11
16/08/2015	Landsat 8 (LDCM)	30	11
18/08/2016	Landsat 8 (LDCM)	30	11
02/06/2017	Landsat 8 (LDCM)	30	11
23/07/2018	Landsat 8 (LDCM)	30	11
14/10/2019	Landsat 8 (LDCM)	30	11

MATERIALS AND METHOD

Shoreline automated delineation from satellite imagery

The methodology adopted in this study (Fig. 3) maps shoreline position changes along the study coastline for two periods (1999–2019 and 1999–2015). Estimation of shoreline change for the period between 1999 and 2015 (2015 being the year of sample collection) was applied to interpret the correlation between shoreline change analysis and the heavy mineral concentration and mean grain size of samples collected alongshore the study area. Additionally, shoreline change between 1999 and 2019 was monitored to assess the impact of Ghalioun fish farm activities constructed after 2015.

Datasets

In the present study, Landsat Enhanced Thematic Mapper Plus on Landsat 7 (Landsat 7 ETM+) and Operational Land Imager (OLI) on Landsat 8 satellite data encountered in (path 177 and row 38) were selected annually covering the period from 1999 and 2019 except 2009 (Table 1, Fig. 4). These series of image data (20 series) are accessible from the USGS Global Visualization Viewer (GloVis, http://glovis.usgs.gov/).

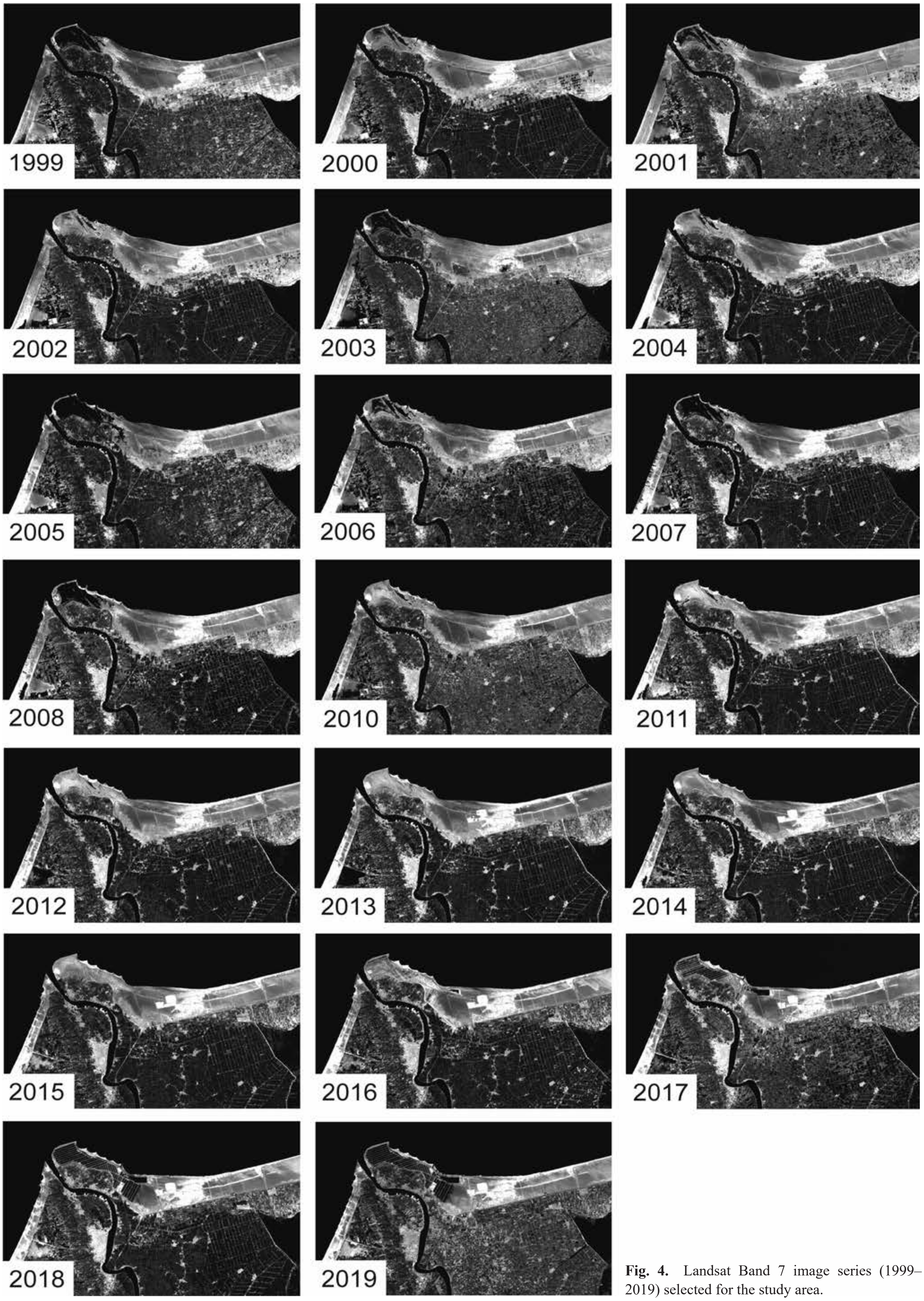

Fig. 4. Landsat Band 7 image series (1999–2019) selected for the study area.

The Landsat series includes the former 13 images (Landsat 7 ETM+) and the most recent images are Landsat 8 OLI, and all images have 30m spatial resolution. Datasets were acquired in close temporal proximity, mostly during the summer, to reduce the seasonal differences. The Landsat images are free of clouds. Fortunately, the tidal range along the study area is very small (20–56 cm); thus, the tidal effect is negligible. The accuracy of the shoreline mapping and land/sea interface mapping depends on the geometrically rectified images.

Image processing

Landsat images used in this study are level 1 terrain-corrected data (LIT), which were radiometrically and geometrically terrain-corrected and ortho-rectified products in the Universal Transverse Mercator (UTM) and World Geodetic System (WGS84) datum, zone 36 north (UTM/zone 36 north, WGS84). For accurate and reliable shoreline monitoring, further systematic correction was applied (Landsat Project Science Office, 2008). To remove atmospheric scattering, atmospheric correction of Landsat images (FLAASH) is a critical step, which was carried out using the radiometric correction tool in ENVI v5.3.Then, the Landsat images were converted into reflectance values. Input data requirements for this step are available in the Landsat metadata documentation.

For the present study, ENVI v5.3 and ArcGIS v10.5 were used for all the image-processing needs. The images from 2004 to 2012 had gaps due to missing data in the SLC-OFF Landsat 7 ETM+. These gaps were filled using the simple gap-filling procedure of ENVI v5.3 (Fig. 5).

The thresholding technique is a segmentation process

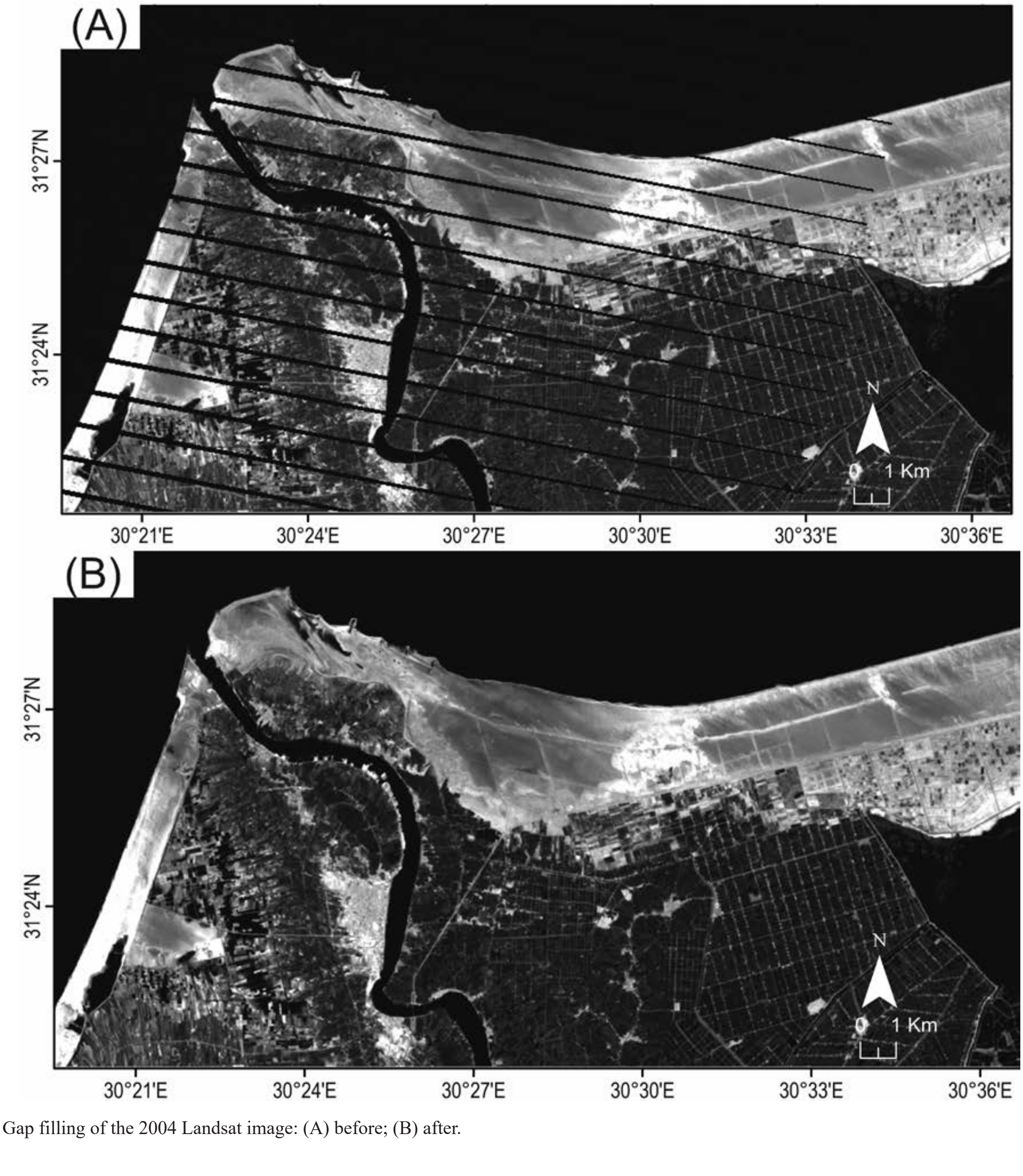

Fig. 5. Gap filling of the 2004 Landsat image: (A) before; (B) after.

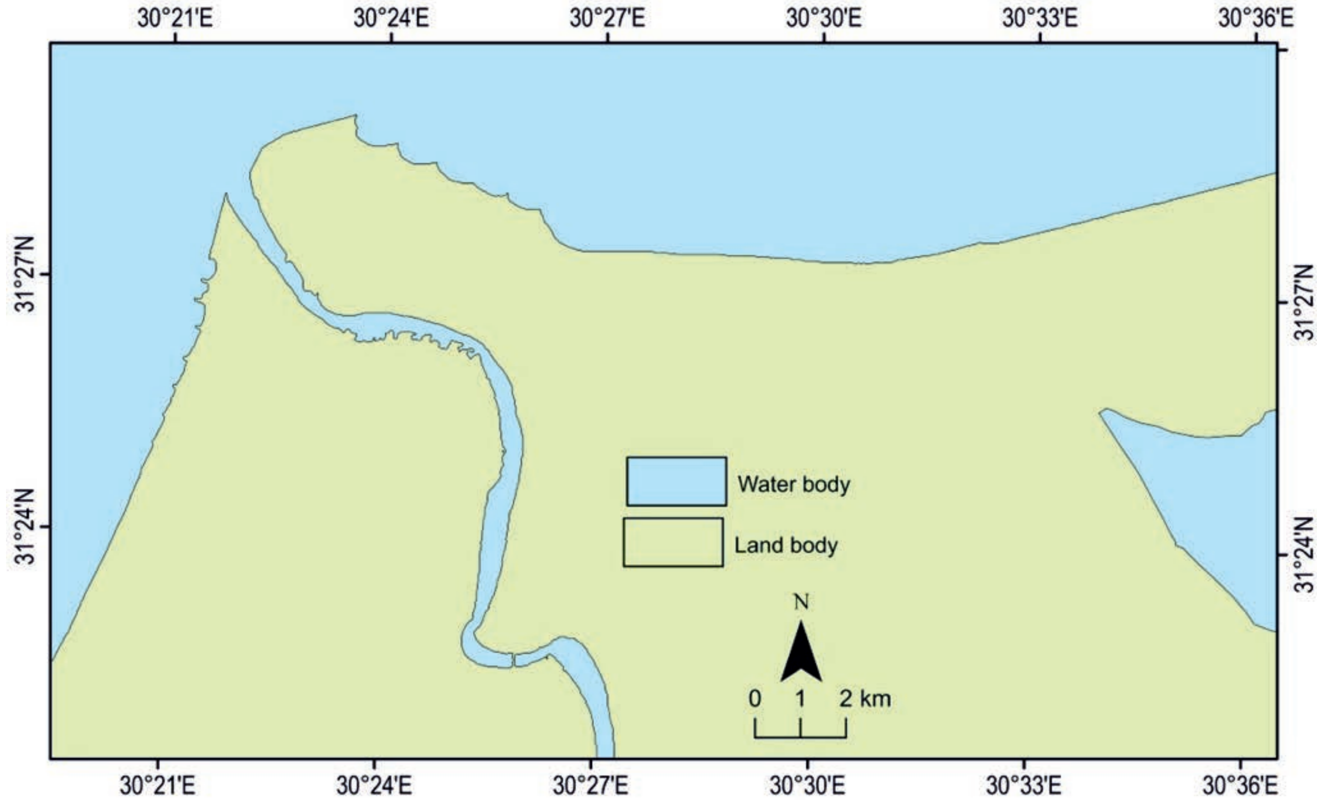

Fig. 6. Binary (mask) image obtained by threshold segmentation of the 2015 Landsat Band 7 image.

in which a threshold value is selected to separate the image into land and water components and delineate the land / sea boundary, referred to as the shoreline, using a histogram. Thresholding values can be set either manually or automatically; a process known as automatic thresholding (Raju and Neelima, 2012). The segmentation procedure was applied to a single-band image (mid-infrared channel, band 7) of ETM+ and OLI sensors. Band 7 of both Landsat sensors was utilised due to the varied spectral behaviour and the spectral response of water and land components at this band.

Within this infrared band, water appears black due to strong absorption, with water reflectance approaching zero. Conversely, the reflectance of land covers is greater than that of water within this infrared band range and appears brighter because of their strong reflectance. By applying histogram thresholding, water and land classes were clearly separated, even in areas of water turbidity caused by longshore sediment transport, in which a sharp boundary was detected between water and land. Consequently, binary images (masked images) were obtained in which water and land pixels were coded as 0 and 1, respectively (Fig. 6).

The binary images (masked images) were then converted into polygon vector layers from which shorelines were extracted. Using ArcGIS version 10.5, the vector layers were processed, and all polygons were converted to lines, resulting in 20 shorelines (Fig. 7). The 20 extracted shorelines were smoothed to reduce their jagged edges and then merged into a single shapefile (Fig. 8).

Computing shoreline rate of change and future projection

A geodatabase was generated containing all derived shorelines. Each shoreline was assigned attributes, including acquisition date, length, identity, shape, and uncertainty. The acquisition date for each image was entered into the date field, while the length, identity, and shape were automatically generated. A baseline was generated with attributes, including shape length, identity, group, offshore, and CastDir, to estimate annual shoreline change rates using the Digital Shoreline Analysis System (DSAS) (Fig. 9).

Digital Shoreline Analysis System (DSAS) version 3.2 is an ArcGIS toolbar developed using GIS as a platform by the United States Geological Survey (USGS) (Thieler *et al*., 2009) to estimate rates of shoreline change and predict shoreline position as a function of time and erosion/accretion rates (Fig. 10).

The mean annual rate of shoreline change was measured for all transects employing the Linear Regression Rate (LRR) statistical approach. LRR values were calculated by fitting a least-squares regression line to all shoreline points for a particular transect (Thieler *et al*., 2009). The LRR approach is the most suitable for estimating long-term rates of shoreline change. This approach does not require any prior information about sediment movement or wave pattern because the cumulative effect of all the underlying processes is assumed to be captured in the shoreline-position history

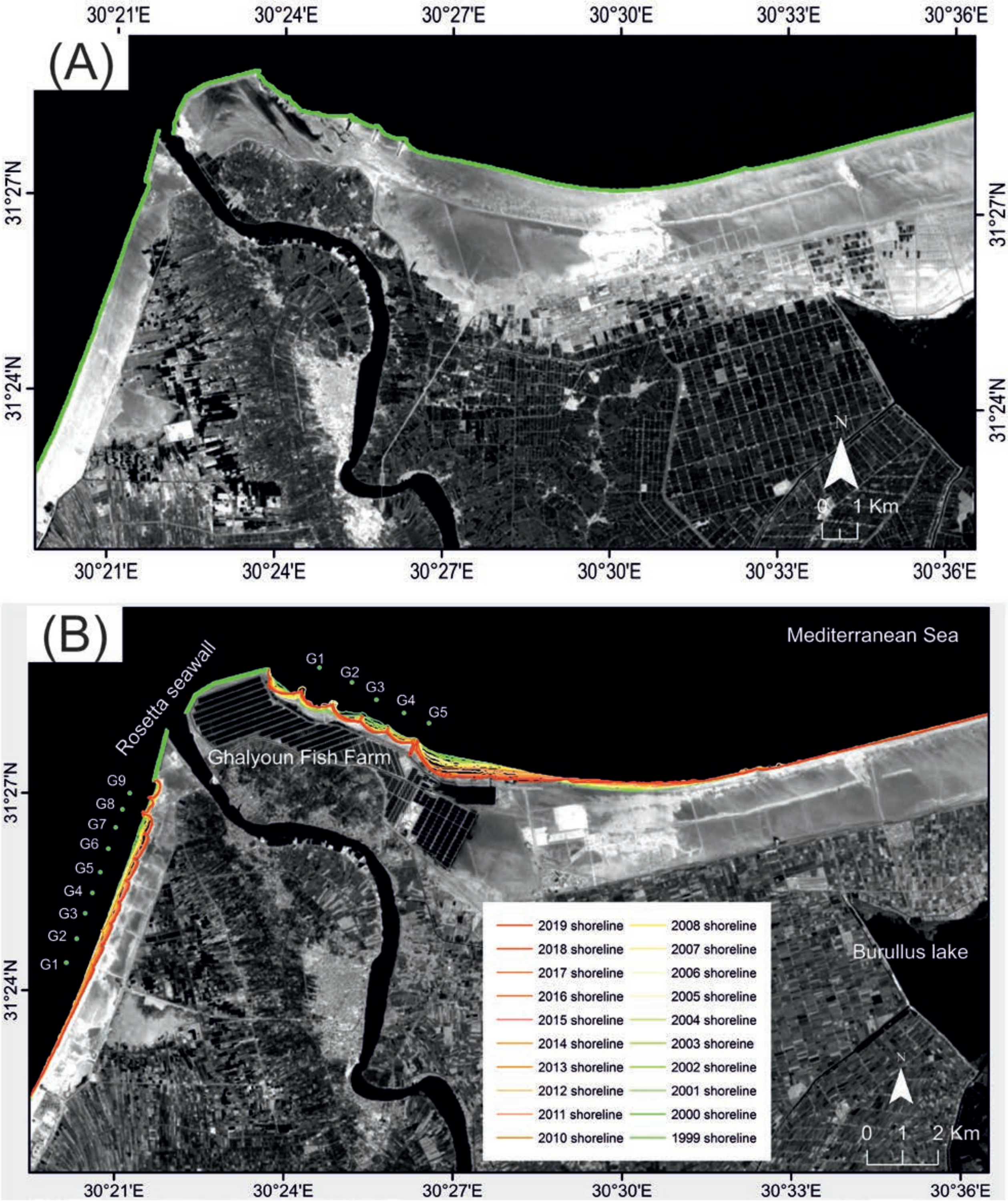

Fig. 7. (A) Shoreline (dark green line) extracted from the 2000 Landsat band 7 image. (B) The 20 shorelines extracted over the study period.

(Li *et al*., 2001). The accuracy of the calculated shoreline-change rate depends on the accuracy of the obtained shorelines, the temporal shoreline changes and the amount of data used. This approach is more precise for predicting future shoreline positions (Fenster *et al*., 1993), so it is adopted in the present study to predict shoreline position for 2030 along the study area.

Beach sediments analysis

Sampling

Beach samples (18 samples) spaced by 1 to 3 km were collected from the beach face sediments at the shoreline along the study area (Fig. 11). Each beach sample was col-

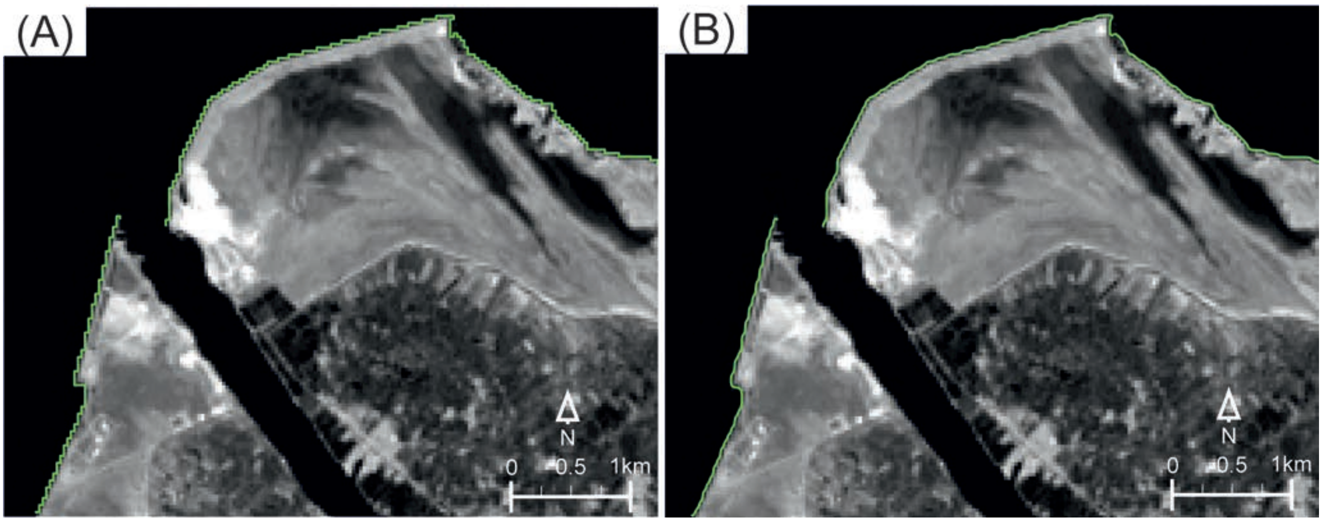

Fig. 8. Smoothing the jagged edge of the shoreline (dark green line): (A) before; (B) after.

Fig. 9. DSAS input data: offshore baseline (dark green line) and 20 extracted shorelines (red lines) for the period 1999–2019.

lected from the upper 15 cm of the sand beach face using a plastic scoop, weighed between 1 and 2 kg and kept in plastic bags. These samples were taken from the "active" layer (15 cm) to capture the most recent hydrometeorological conditions (Pupienis *et al*., 2011). The positioning of each station was determined using a GPS. The sediment samples were air- and sun-dried, and the disaggregation of coherent sediment was done. A representative sample was obtained for grain-size analysis and heavy minerals separation, while the remaining sediments were stored in plastic bags as reference samples.

Grain-size analysis

The mean grain sizes (M_z) were adopted from Elsherif *et al*. (2020). The associated sampling and analytical methodology is described therein.

Mineralogical analysis

The 2–3 phi (250–125 μm) and 3–4 phi (125–63 μm) (fine sand and very fine sand) fractions were selected for

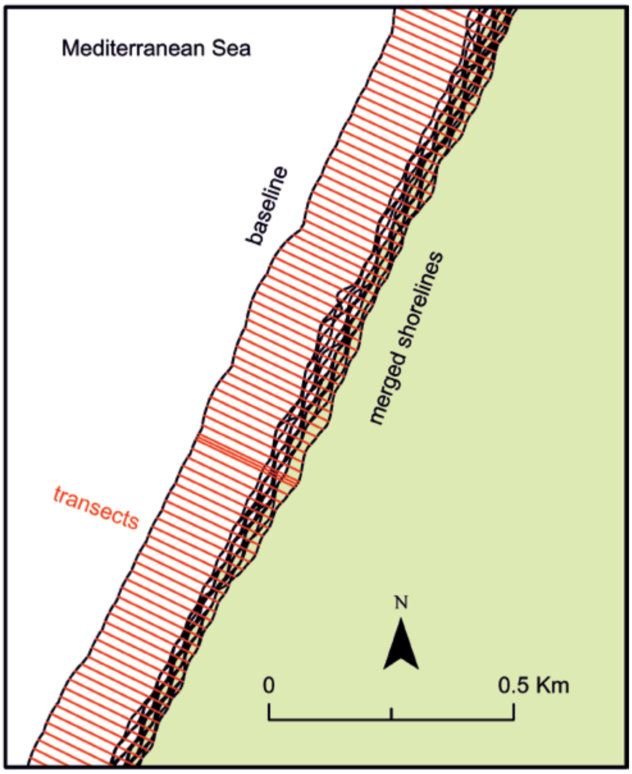

Fig. 10. DSAS-generated transects (n = 1838) cast perpendicular to the baseline at 20 m intervals.

heavy-minerals separation in beach sediments. The samples were kept in a beaker filled with distilled water at room temperature for a day to dissolve soluble salts. The samples underwent acid digestion to remove carbonates and degrade salts using 10% dilute HCL, followed by a rinse with distilled water to dissolve soluble salts. The samples were then treated with dilute hydrogen peroxide (H_2O_2; 30%) to remove the organic matter, washed at least three times with deionised water and dried in the oven.

The heavy liquid method was applied to separate heavy minerals using bromoform (Sp.gr. 2.89 g/cm^3), and the specific gravity was checked before each use, following the procedure outlined in Milner *et al*. wools(1962). Sample fractions were added to bromoform in a separating funnel supported with a glass tap, which feeds into another funnel topped with filter paper. To avoid mass-trapping effects, the samples were stirred occasionally, and approximately 20 minutes were enough to settle the heavy minerals (<2.89 g/cm^3). The heavy-mineral separate was drained onto filter paper and washed with acetone to remove any residual bromoform from grains. Next, the filter papers containing the separates were placed in bowls and air-dried at room temperature for 2 hours. The heavy mineral amounts were estimated and expressed as weight percentages of the total heavy minerals content (HM). Spatial variations in heavy minerals concentrations provide an overview of the distribution patterns.

RESULTS

Estimated shoreline change for the study area during the period from 1999 to 2019

For convenience in estimating shoreline change, the study area was subdivided into three beach sectors (A, B, and C) (Fig. 12A) based on natural and artificial alongshore discontinuities caused by discontinuities in longshore sediment transport. The western sector A is approximately 10 km long, extending from the western seawall to the westernmost point in the study area. Sector B extends 18 km eastward from the eastern seawall. Sector C is approximately 4 km long and consists of the sand bar separating Burullus Lake from the Mediterranean Sea.

The rates of shoreline change using the LRR approach were calculated for each transect over the entire study period (1999–2019) and presented (Fig. 12, Table 2). The

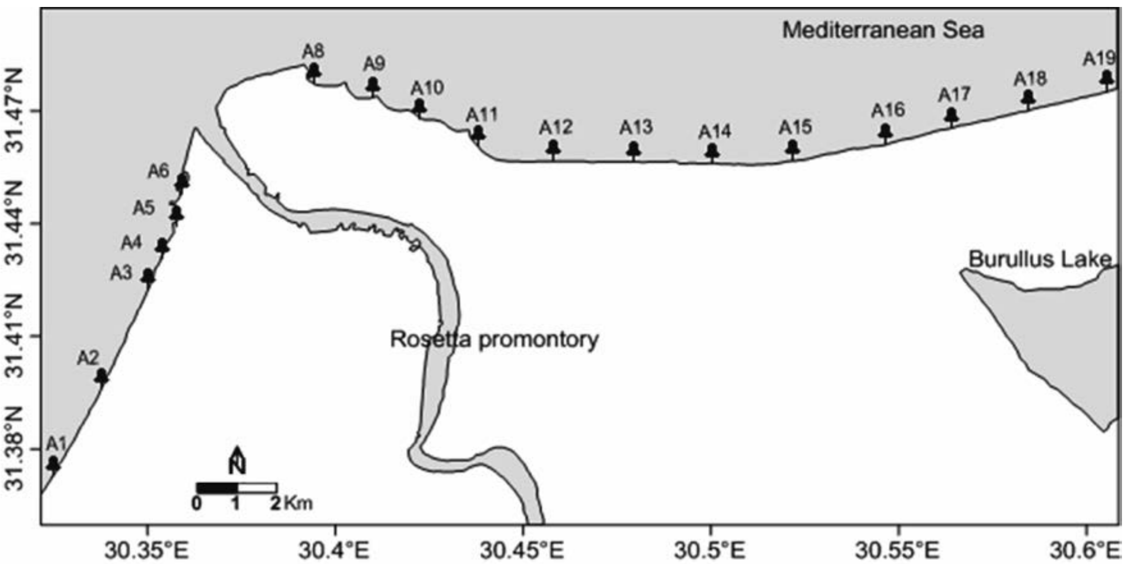

Fig. 11. Sampling sites located west and east of the Rosetta Promontory.

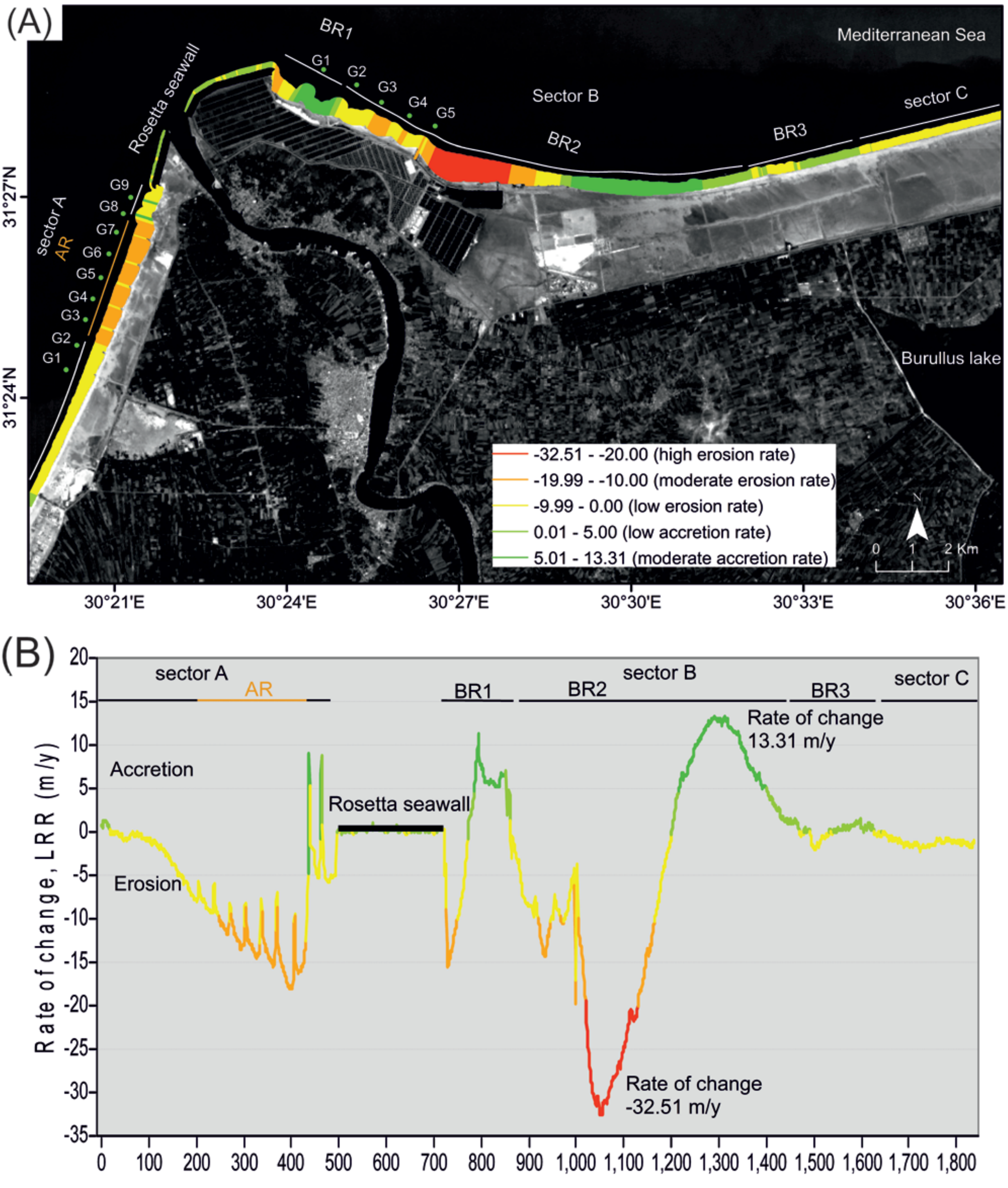

Fig. 12. (A) Eroding and accreting coastal sectors between 1999 and 2019, with maximum erosion observed downdrift of G5. (B) Shoreline change rates (LRR; m/year) estimated alongshore for the period 1999–2019.

mean rate of shoreline change was -3.65 m/year, with a mean rate of erosion of 7.92 m/year and a mean rate of accretion of 4.02 m/year. Approximately 69.40% of the study coastline experienced erosion at varying rates, covering approximately 22.2 km. Additionally, areas experiencing significant erosion accounted for 50.49% of the coastline, while areas exhibiting significant accretion accounted for 20.24%. The coastline west of the western seawall (sector A) experienced erosion (95%), covering approximately 9.5 km. Erosion affected 12.7 km (57.70%) of the coastline east of the eastern seawall (sectors B and C). The seawall area exhibited almost no change.

Erosion was concentrated at varying degrees in sector A, with a mean shoreline change rate of -6.09 m/year (Fig. 12). The highest shoreline retreat within the sector was 18 m/year, concentrated immediately downdrift of the

Table 2. Shoreline change rates by Coastal Sector (LRR; m/year) and percentages of eroding and accreting zones along the study coastal sectors during the two study periods. Abbreviations: LRR, Linear Regression Rate; m/y, metres per year; sig., significant.

Sector / Segment	1999–2019			1999–2015		
	Mean Change	Erosion	Accretion	Mean Change	Erosion	Accretion
Whole Area (~32 km)						
Mean (LRR, m/y)	-3.65	7.92	4.02	-3.49	8.65	4.45
Land under erosion /sig.erosion /sig. accretion:	*69.40%*	*50.49%*	*20.24%*	*64.30%*	*44.61%*	*21.38%*
Sector A (~10 km) – LRR (m/y)						
Mean change / Highest erosion / Highest accretion	-6.09	18.00	8.90	-6.85	19.45	8.76
Land under erosion:	*95% (1999–2019)*			*86% (1999–2015)*		
Sector B (~18 km) – LRR (m/y)						
Mean change / Highest erosion / Highest accretion	-3.40	32.51	13.31	-3.11	35.87	15.86
Land under erosion:	*48% (1999–2019)*			*44% (1999–2015)*		
└─ Segment BR1 (~2.7 km)						
Mean change / Highest erosion / Highest accretion	0.20	15.62	11.28	0.68	15.81	13.33
Moderate erosion and accretion · Seawall interception of eastward longshore drift						
└─ Segment BR2 (~10.8 km						
Mean change / Highest erosion / Highest accretion	-6.07	32.51	13.31	-5.96	35.87	15.86
Highest rates in study area – downdrift 5th eastern groin						
└─ Segment BR3 (~4.6 km)						
Mean change / Highest erosion / Highest accretion	0.69	2.04	4.97	1.30	1.63	4.94
Land under erosion:	*22% (1999–2019) · ~1.0 km*			*11% (1999–2015) · ~0.6 km*		
Sector C (~4 km) – LRR (m/y)						
Mean change / Highest erosion / Highest accretion	-1.11	2.22	0.05	-1.00	1.99	0.00
Land under erosion:	*~100% (1999–2019)*			*~100% (1999–2015)*		

seventh western groyne. The highest shoreline advance of 8.9 m/year occurred at the eighth western groyne. Segment AR (3.7 km long), which represents about 37% of the sector length and extends between the second and the eighth western groynes (Fig. 12a), experienced moderate erosion rates interspersed with areas of low erosion/accretion in the updrift sides of the groynes. The farthest-westward beach area experienced limited changes; it remained relatively stable and turned to accretion at the farthest western point.

From 1999 to 2019, sector B exhibited erosion and accretion zones on the leeside of the seawall, with a mean shoreline change rate of -3.4 m/year. The highest shoreline retreat of 32.51 m/year and the highest shoreline advance of 13.31 m/year were observed; both were immediately downdrift of the fifth eastern groyne and represent the extreme values in the whole study area. Erosion affected approximately 8.7 km of the sector coastline at varying rates, accounting for 48.3% of the total length.

The first segment (BR1) extends from the eastern seawall to the second eastern groyne, and is 2.7 km long, representing 15% of sector B length (Fig. 12a). It experienced low-to-moderate erosion and accretion rates at a mean shoreline change of 0.20 m/year. The highest erosion and accretion rates within this segment were 15.62 m/year and 11.28 m/year, respectively (Table *2*).

Meanwhile, the second segment (BR2) within sector B, 10.8 km long, experienced the highest erosion rate (32.51 m/year) and the highest accretion rate (13.31 m/year) in the entire study area (Fig. 12). The segment is under erosion with a mean shoreline change of -6.07 m/year. The beach area between the second and fifth eastern groyne experienced low to moderate erosion, with the highest rate observed immediately downdrift of the fifth eastern groyne.

The third segment (BR3) is approximately 4.6 km long and experienced only limited shoreline change. It is characterised by low erosion and accretion rates, with the highest retreat rate of 2.04 m/year and the highest accretion rate of 4.97 m/year, and a mean change rate of 0.69 m/year (Fig. 12, Table *2*). Approximately 22% of the segment length exhibited erosion, covering approximately 1 km.

Erosion occurred at low rates in the third sector C, with the highest erosion rate of 2.22 m/year, the highest accretion rate of 0.05 m/year and a mean shoreline change of -1.11 m/year (Fig. 12, Table *2*).

Projection of 2030 shoreline

Using the shoreline change rates (LRR, m/year) from the 1999–2019 study, the 2030 shoreline is predicted with the shoreline forecasting option in DSAS. The coastline is predicted to recede by a mean distance of 108 m. Furthermore, the featured eroded areas would lose an additional area of 2.24 km^2 by 2030; the western side of the promontory would lose approximately 0.8 km^2, while the eastern side would suffer an extreme loss of 1.4 km^2. The accreted areas would increase by 0.74 km^2; most of it would be in the eastern sector (0.73 km^2). The area downshore of the fifth eastern groyne would experience the greatest erosion and would lose a further distance of 519 m. The adjacent embayment, situated eastward, would add the highest accretion distance, up to 207 m (Fig. 13).

Fig. 13. Projected shoreline position in 2030 (red line), assuming no further coastal changes.

Quantified shoreline change for the study area during the period from 1999 to 2015

The shoreline change between 1999 and 2015 was estimated along the study coastline at a mean of -3.49 m/year. The mean erosion rate was estimated to be 8.65 m/year, and the mean rate of accretion is 4.45 m/year (Fig. 14, Table *2*). The study coastline experienced varying degrees of shoreline retreat, with approximately 64.3% affected, covering a distance of approximately 20.6 km. Erosional areas exhibited significant rates, affecting 44.61% of the coastline, while areas that underwent significant accretion accounted for 21.38%. No change was observed along the seawalls.

Erosion affected 86% of the western coast sector and 54.5% of the eastern coast sector, extending approximately 8.6 km and 12 km, respectively. During 1999–2015, sector A revealed shoreline change at a mean of -6.85 m/year and sustained low to moderate degrees of erosion (Fig. 14). The highest shoreline retreat of 19.45 m/year was observed downdrift of the seventh western groyne, while the utmost shoreline advance of 8.76 m/year was situated at the eighth western groyne.

Overall, sector B showed erosion and accretion patterns at a mean shoreline change rate of -3.11 m/year (Fig. 14). Shoreline retreat reached its extreme at 35.87 m/year. The highest shoreline advance observed along the entire study area of 15.86 m/year was positioned downdrift of the fifth eastern groyne. Shoreline retreat extended about 8 km and covered approximately 44.4% of the sector length.

Segment BR1 experienced an intense erosion rate of 15.81 m/year and a high accretion rate of 13.33 m/year at a mean change of 0.68 m/year. Meanwhile, segment BR2 showed the highest erosion and accretion rates in the whole study area at a mean change of -5.96 m/year. The beach area downdrift of the fifth eastern groyne experienced the highest erosion rate of 35.87 m/year and the highest accretion rate of 15.86 m/year (Fig. 14). Segment BR3 experienced a shoreline retreat of 1.63 m/year and an advance of 4.94 m/year at a mean change of 1.30 m/year. It encountered erosion along 600 m (10.9% of its length).

Sector C totally experienced erosion at a high rate of 1.99 m/year, with no accretion rates and a mean shoreline change of -1 m/year (Fig. 14).

Table 3. Mean grain size (Φ-scale; Elsherif *et al.*, 2020) and heavy mineral (HM wt.%) variability in the sediment distribution. Abbreviations: M.S., medium sand; F.S., fine sand.

Sample number	M_z (Φ) (mean size)		Total HM wt.%	Sample number	M_z (Φ) (mean size)		Total HM wt.%
A1	1.79	M.S.	0.71	A11	2.44	F.S.	7.31
A2	2.38	F.S.	4.10	A12	2.30	F.S.	2.47
A3	2.56	F.S.	19.27	A13	2.49	F.S.	9.07
A4	2.47	F.S.	15.37	A14	2.50	F.S.	7.31
A5	2.46	F.S.	10.77	A15	2.47	F.S.	5.01
A6	2.47	F.S.	17.48	A16	2.46	F.S.	5.37
A8	2.51	F.S.	23.14	A17	2.52	F.S.	9.25
A9	2.01	F.S.	2.62	A18	2.51	F.S.	7.03
A10	2.52	F.S.	19.40	A19	2.56	F.S.	8.87
Mean value	2.42	F.S.	10.12				

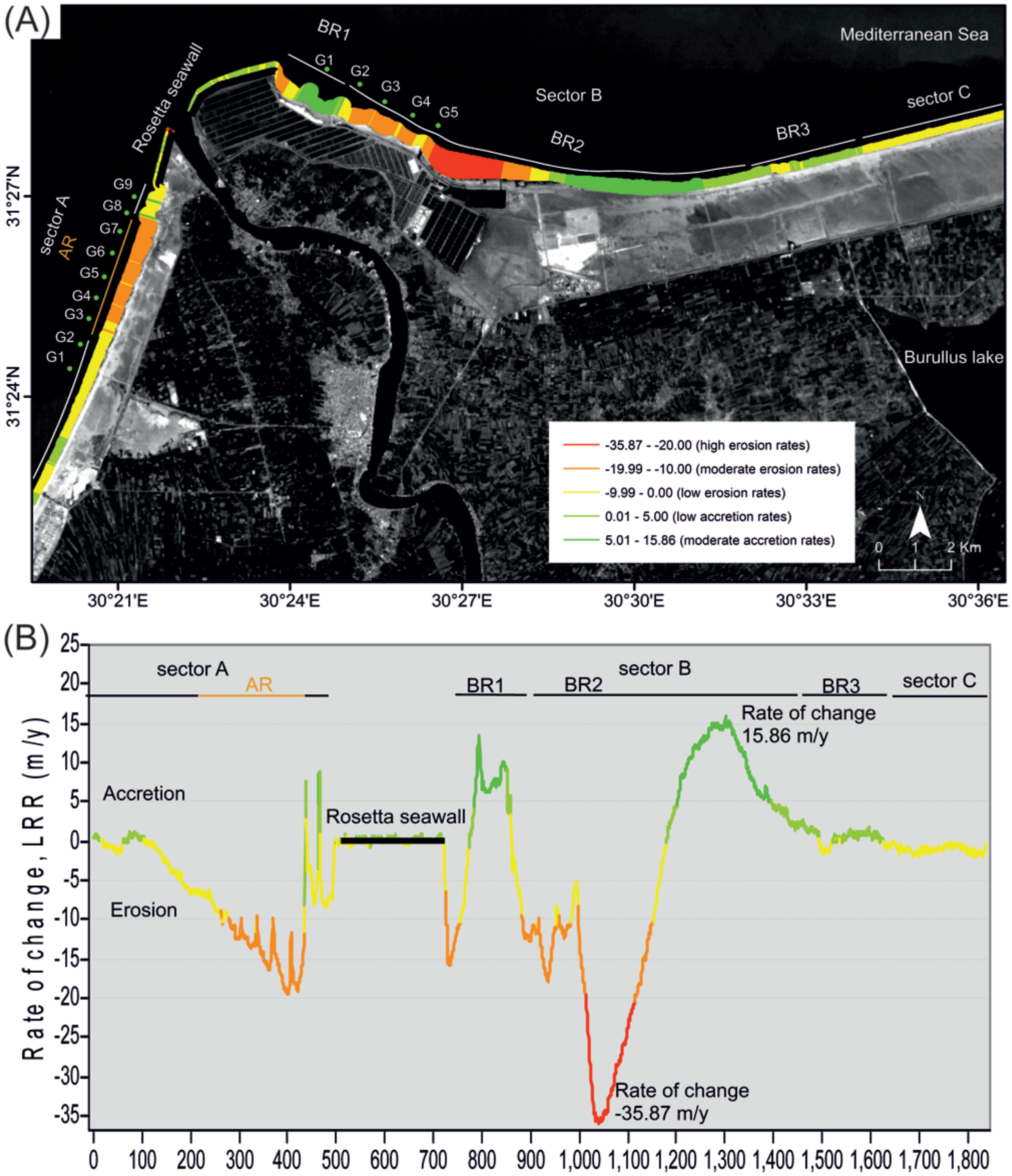

Fig. 14. (A) Alongshore erosion and accretion patterns in the study area between 1999 and 2015. (B) Alongshore shoreline change rates (LRR; m/year) for the period 1999–2015.

Assessment of trends in longshore sediment patterns, heavy minerals and texture interrelationships.

The calculated mean values, adopted from the previous study, ranged from 1.79 Φ (medium sand) to 2.56 Φ (fine sand), with a mean of 2.42 Φ (fine sand) (Table 3, Elsherif *et al*., 2020).

The total heavy mineral (HM) concentration detected in all samples collected along the shoreline ranged between 0.71 wt.% (site A1) and 23.14 wt.% (site A8), with a mean value of 10.21 wt.% (Table 3).

We examined the statistical relationship between the shoreline change rate during the period 1999 to 2015 and heavy mineral concentration and mean grain size of sam-

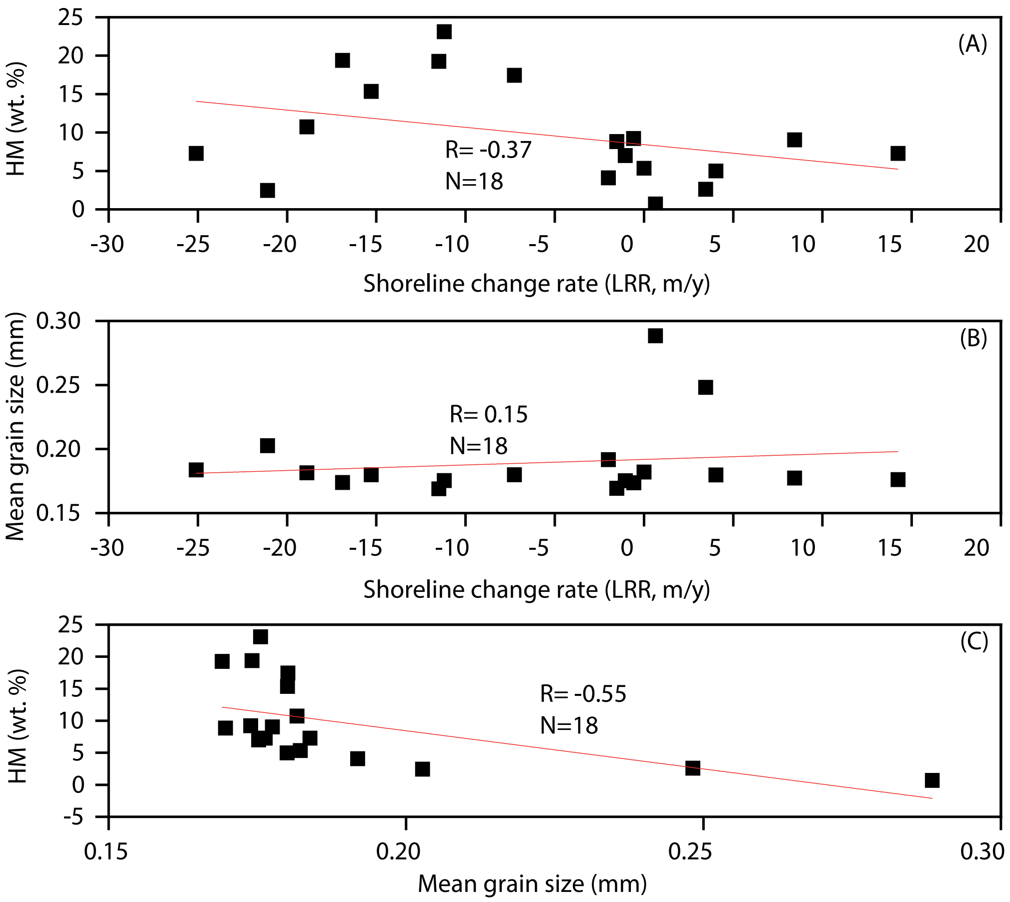

Fig. 15. Statistical relationships between (A) shoreline change rates and heavy mineral concentration. (B) shoreline change rates and mean grain sizes (C) mean grain sizes and heavy mineral concentration.

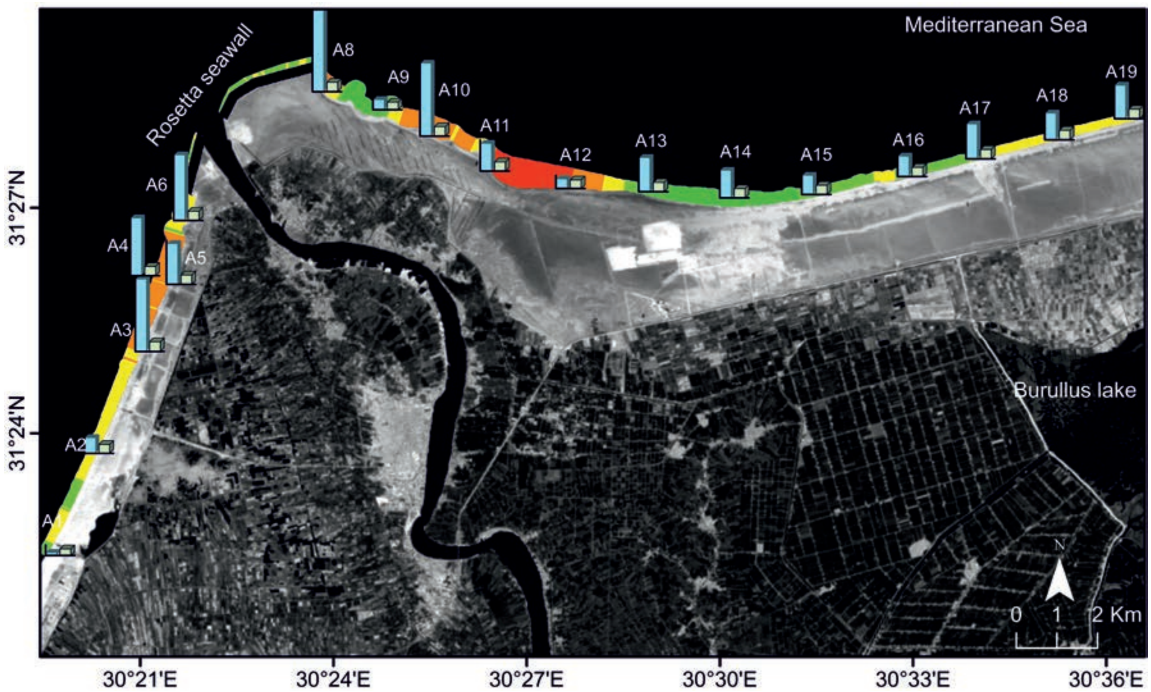

Fig. 16. Distributions of heavy mineral concentrations (blue bars; HM wt%) and mean grain size (light green bars) alongshore within erosion and accretion patterns for the 1999–2015 study period (for explanations, see Fig. 13).

ples of shoreline sediment (Fig. 15). Additionally, the spatial longshore distributions of erosion and accretion patterns, heavy mineral concentration, and mean grain sizes were presented (Figs. 16, 17).

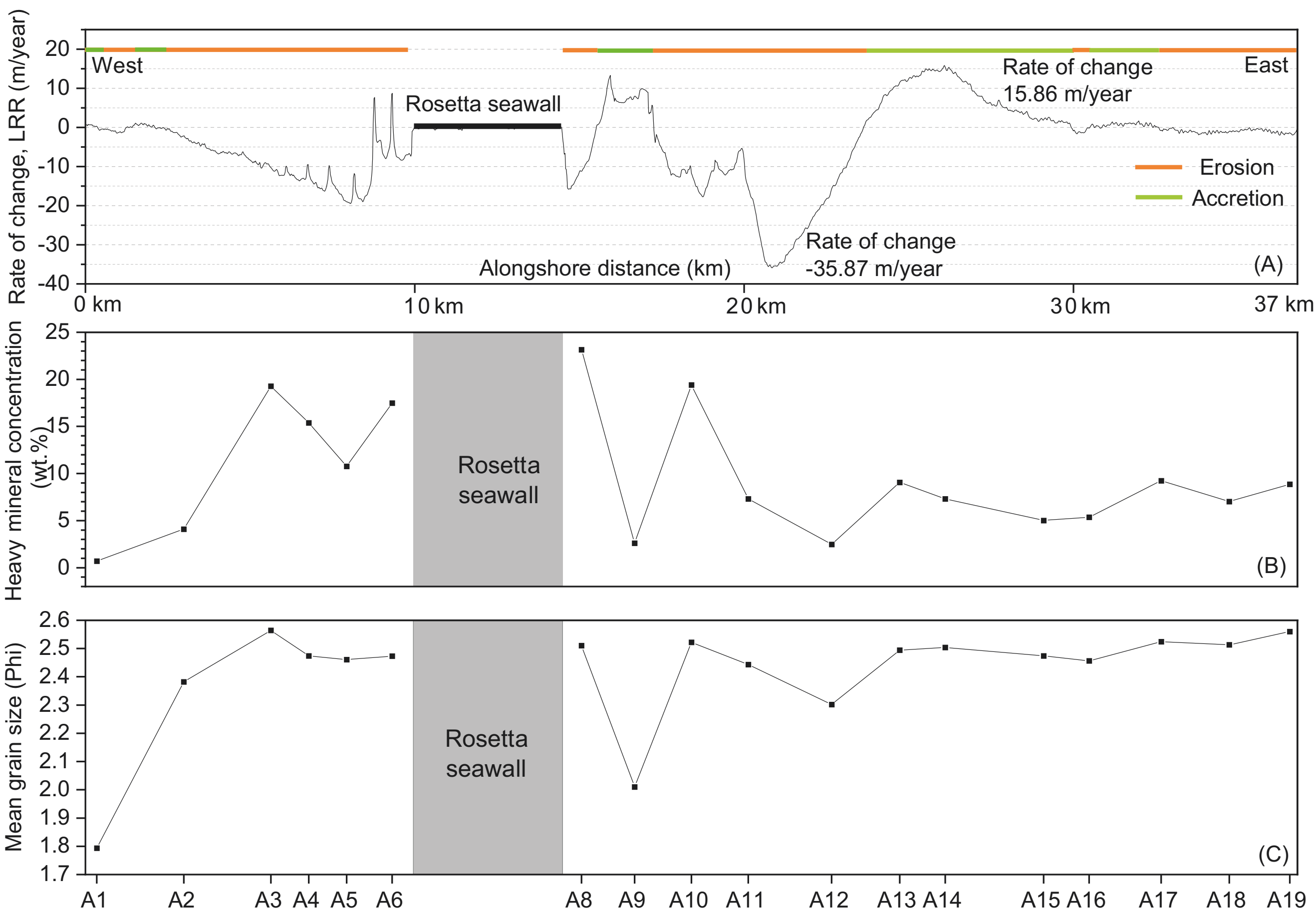

Fig. 17. Longshore distributions of (A) shoreline change rates (B) heavy mineral concentrations in shoreline samples (C) mean grain sizes of shoreline samples.

The scatter plot of heavy mineral concentration and shoreline change rates revealed a weak negative relationship, with a correlation coefficient (R) of -0.37. The relationship between shoreline change rates and mean grain sizes is very weak (R = 0.15), with almost negligible correlation. The relationship between mean grain size and heavy mineral concentration is a moderate negative (R= -0.55).

DISCUSSION

Shoreline Change 1999–2019

Shoreline change analysis along the Rosetta coastline during 1999–2019 shows a dominantly erosional trend, with erosion dominating nearly 70% of the investigated shoreline at a mean rate of -3.65 m/year (Fig. 12, Table 2). The widespread occurrence of significant erosion indicates that the coastal system is operating under a negative sediment budget. This pattern is consistent with the well-documented sediment starvation affecting the Nile Delta coast following the construction of the High Aswan Dam and upstream barrages, which have drastically curtailed fluvial sediment supply to the Mediterranean coast (Stanley and Warne, 1993; Frihy and Lawrence, 2004). The spatial variability in erosion and accretion across the three sectors, however, reflects the superimposed influence of anthropogenic coastal structures, particularly seawalls and groynes, on the residual littoral drift system. Under such circumstances, coastal processes are unable to compensate for sediment losses, resulting in continuous shoreline retreat along extensive stretches of the study area.

The western sector (A) exhibited a mean shoreline retreat of -6.09 m/year across 95% of its ~10 km length (Fig. 12, Table 2). The dominant driver of this retreat is the combined influence of sediment starvation and the interruption of longshore sediment transport by the western seawall. The western seawall compounds the dam-induced sediment deficit by blocking the residual west-southward longshore sediment flux from reaching downdrift beaches. The updrift flanks of successive groynes locally trapped a fraction of the mobilised sediment, producing alternating low-erosion and limited-accretion cells. This behaviour is consistent with the expected updrift impoundment and downdrift erosion pattern classically associated with groyne fields (Komar, 1998). Nevertheless, even within AR, erosion remained the dominant net trend, underlining that local structural retention cannot compensate for the region-wide sediment deficit.

Sector B displayed a more complex pattern and was subdivided into three segments (BR1, BR2, and BR3) (Fig. 12); each segment represents a cycle of erosion, eastward longshore sediment transport and accretion. The erosion patterns of segment BR1 are primarily attributed to the eastern seawall. The eastern seawall acts as a structural barrier that intercepts sediment moving within the eastward-directed longshore transport pathway. Consequently, the natural sediment flux that would otherwise nourish the beaches downdrift of the structure is deflected and impounded, leaving the lee-side coastline in a state of sediment deficit. The eroded material mobilised within BR1 is captured by the adjacent embayment through the easterly longshore drift, producing the moderate accretion rates observed downdrift.

Segment BR2 (~10.8 km) exhibited the most extreme shoreline dynamics in the entire study area, with the highest erosion and accretion rates, both located downdrift of the fifth eastern groyne (Fig. 12, Table 2). The construction of successive groynes along this segment has primarily accelerated net land loss by disrupting the continuity of sediment flux along the shore, thereby generating localised zones of erosion and accretion. Groyne fields can enhance cross-shore sediment losses by intensifying local circulation cells and promoting offshore transport. The large quantities of eroded material mobilised within BR2 were subsequently transported eastward in the dominant longshore direction and deposited in sinks proximal to the erosion sources, generating the high localised accretion rates observed. The observed depositional areas further support the existence of an active eastward littoral drift system driven primarily by prevailing northwestern wave conditions. This pattern of erosion source-proximal sink coupling is characteristic of high-energy littoral environments with a well-defined net drift direction (Komar, 1998; van Rijn, 2011), and demonstrates that the groyne field, rather than contributing to shoreline instability, has locally reorganised and chronically intensified the erosion-deposition cycle.

Segment BR3 and Sector C both exhibited markedly subdued shoreline dynamics, with mean change rates of +0.69 m/year and -1.11 m/year, respectively (Fig. 12, Table 2). The near-stability of BR3 likely reflects the dissipation of longshore energy and the partial sequestration of sediment transported from the more active western segments. Sector C was subject to limited wave exposure and constrained sediment exchange, producing the observed low erosion rates (maximum -2.22 m/year) with negligible accretion (+0.05 m/year). This sector nonetheless remains vulnerable to long-term erosion given the absence of a meaningful sediment source and the projected progressive sea-level rise in the eastern Mediterranean (Marriner *et al*., 2012).

The 2030 shoreline projection further emphasises that current erosion processes are likely to continue if existing environmental and management conditions persist. The forecasted mean recession of 108 m and net land loss of 2.24 km² reflect a strongly negative sediment budget, with the eastern flank of the Rosetta promontory bearing the greatest projected loss (~1.4 km²) (Fig. 13). The extreme erosion of 519 m projected downdrift of the fifth eastern groin, offset only partially by 207 m of accretion in the adjacent embayment, further demonstrates that existing groyne infrastructure redistributes rather than mitigates sediment losses. The modest projected accretion of 0.74 km² remains insufficient to compensate for the substantially larger erosional deficit across the study area. These projections represent a conservative minimum-bound estimate, as the mean erosion rate of -3.65 m/year was established before the full operational impact of the Grand Ethiopian Renaissance Dam (GERD), whose sediment retention is expected to further deplete the already starved Nile Delta littoral system. Unless integrated coastal management measures, including beach nourishment and structural reconfiguration, are implemented, land loss along this coastline will continue to accelerate, threatening the coastline and the communities and infrastructure it supports.

Shoreline Change 1999–2015

The shoreline change analysis for the 1999–2015 period yielded a mean retreat rate of -3.49 m/y, broadly consistent with the longer 1999–2019 record (-3.65 m/y) (Fig. 14, Table 2), confirming that the erosional trend along the Rosetta coast is a persistent, structurally driven phenomenon rather than a temporally isolated event. Approximately 64.3% of the study coastline experienced retreat during this period, with significant erosion accounting for 44.61% of the total length, values that closely mirror the 1999–2019 statistics and reinforce the stability of the erosional signal over time.

Sector A continued to be the most erosion-dominated sector, with a mean retreat of -6.85 m/year and 86% of its length experiencing regression (Fig. 14, Table *2*). The spatial pattern of maximum erosion (19.45 m/year) downdrift of the seventh western groin and localised advance (8.76 m/y) at the eighth groyne is consistent with the groyne-field dynamics described for the full study period. Notably, the peak erosion rate of 19.45 m/year recorded during 1999–2015 exceeds that of the full 1999–2019 period (18 m/year), suggesting a marginal deceleration in maximum retreat rates within the western sector toward the end of the study span.

Sector B reproduced the erosion-sediment transport-accretion cycling observed over the longer period, with the fifth eastern groin again acting as the focal point of the most extreme shoreline dynamics in the entire study area (Fig. 14, Table *2*). The eastern seawall's obstruction of sediment entry into the eastward longshore drift system remained the primary driver of erosion within segment BR1, producing maximum retreat and deposition rates of 15.81 m/year and 13.33 m/year, respectively. Segment BR2 recorded the highest erosion rate (35.87 m/year) and accretion rate (15.86 m/year) in the whole study area, both located downdrift of the fifth eastern groin. These findings are closely consistent with Ghoneim *et al*. (2015), who documented erosion rates of 30.8 m/year at the same position through 2012, affirming the reliability and continuity of the erosional signal at this hotspot. Segment BR3 exhibited subdued dynamics with a maximum retreat of 1.63 m/year and advance of 4.94 m/year, with only 600 m (~10.9%) of its length under erosion. Sector C recorded complete erosion dominance with a maximum rate of 1.99 m/year, no measurable accretion, and a mean change of -1.0 m/year.

Comparative Analysis Between Study Periods

A cross-period comparison between the 1999–2015 and 1999–2019 datasets revealed important insights into the evolving dynamics of the Rosetta coastline and the influence of post-2015 engineering interventions. While the total length of the erosional coastline expanded between the two periods from ~20.6 km (64.3%) to ~22.2 km (69.4%) (Table 2), the mean erosion rate and peak erosion and accretion values were consistently higher during the shorter 1999–2015 period. This apparent paradox, whereby the spatial extent of erosion increased while peak rates decreased, points to a spatial spreading of moderate erosion at the expense of extreme localised retreat, likely reflecting the partial redistribution of sediment dynamics induced by the Ghalioun fish farm constructed after 2015 and opened in 2017.

The retreat in peak erosion from 35.87 m/year (1999–2015) to 32.51 m/year (1999–2019) and peak accretion from 15.86 m/year to 13.31 m/year (Table 2) within Segment BR2 is most plausibly attributed to the sediment-retaining effect of the Ghalioun fish farm, which extends approximately 4.5 km eastward from the eastern seawall. By partially intercepting the eastward longshore sediment flux, the bond appears to have moderated the extreme erosion-accretion cycle previously concentrated around the fifth eastern groyne, reducing the intensity of localised sediment loss and proximal redeposition without, however, reversing the background erosional trend. This interpretation is consistent with the observed expansion of the erosional coastline length over the same period, as the bond's influence effectively redistributes rather than eliminates the sediment deficit across a wider coastal stretch.

In Segment BR3, the erosional footprint grew from ~600 m (10.9%) during 1999–2015 to ~1 km (21.7%) during 1999–2019, with maximum retreat increasing from 1.63 m/year to 2.04 m/year (Table 2). Similarly, Sector C recorded an increase in maximum erosion from 1.99 m/year to 2.22 m/year between the two periods, with erosion remaining total and no accretion developing. These progressive increases in the eastern and distal sectors suggest that the erosional signal is propagating eastward through the littoral system over time, consistent with a sediment deficit that is both deepening and spatially extending under continued Nile starvation conditions.

Longshore Sediment Patterns, Heavy Mineral and Grain Size

The analysis of longshore sediment patterns, heavy mineral concentrations, and grain size distributions along the Rosetta coastline revealed a complex interplay of hydrodynamic, morphological, and anthropogenic controls that collectively govern the spatial variability of sediment composition and its relationship to shoreline change dynamics. The mean grain-size values (Table 3) indicate a relatively uniform fine-sand-dominated littoral environment along the study coastline. This narrow textural range is characteristic of wave-dominated deltaic shorelines subjected to prolonged hydrodynamic sorting, and is consistent with the well-sorted Nile-derived fine-to-medium sand signature documented along the broader Egyptian Mediterranean coast (Komar, 1998; Frihy and Komar, 1993). The limited textural variability observed between sampling sites further suggests that spatial differences in wave energy and transport intensity along this coastline are insufficient to produce marked grain-size differentiation at the scale of the study area.

The majority of sampled locations yielded HM grades exceeding the 2 wt.% economic viability threshold established in the literature (Table 3) (Behera, 2003; Ravindra Kumar and Sreejith, 2010; Anil Cherian *et al*., 2011), confirming that the shoreline deposits of the study area constitute economically viable beach placer accumulations with promising potential for local industrial exploitation and exportation.

The spatial distribution of HM concentrations is strongly modulated by proximity to the Rosetta promontory, thereby forming a high-resolution geodynamic signature and serving as the primary point source of heavy-mineral-enriched Nile-derived sediments entering the littoral system. Samples collected in the vicinity of the promontory recorded the highest HM grades (Fig. 16), with concentrations diminishing progressively in both eastward and westward directions with increasing distance from the source. This spatial decay pattern is consistent with dilution and selective sorting during longshore transport, identifying the Rosetta estuary as the principal supplier of heavy mineral concentrates to the regional deposit. The relatively uniform HM concentrations observed over the ~12 km stretch east of the promontory (sites A13–A19; 5–9.25 wt.%) reflect a zone of limited active sedimentary processes and smooth coastal morphology, where longshore transport energy is insufficient to generate significant mineralogical differentiation.

The anomalously low HM concentration at site A1 (Fig. 16) is attributable to the coarse-grain mixture at this location, where shell fragment addition results in >500 µm fractions constituting 71.1% of the bulk sediment, effectively diluting the heavy mineral signal through textural coarsening. The localised HM minimum at site A9, positioned on the updrift side of the second eastern groin and flanked by higher-concentration samples (A8 and A10) at downdrift positions, is explained by the preferential accumulation of light, coarse-grained sediment on groin updrift flanks, where reduced transport competence favours deposition of lower-density, coarser fractions. The grain-size distribution of sample A9, with 50% of the sediment in the >500 µm fraction (Fig. 16), corroborates this interpretation and simultaneously reflects the localised influence of the coastal protective structures. These structural anomalies in both granulometry and mineralogy highlight the capacity of engineering infrastructure to imprint detectable signatures on the littoral system's sediment composition, independent of the ambient hydrodynamic regime.

The weak negative relationship between HM concentration and shoreline change rate (R = -0.37) (Fig. 15) reflects the tendency for higher HM grades to be associated with erosional settings (Fig. 16, 17), where preferential removal of lighter quartz fractions through lag concentration progressively enriches residual beach sediments in denser heavy mineral phases. Conversely, lower HM concentrations correspond to accretional zones, where influxes of lighter, quartz-dominated sediment reduce the heavy-mineral concentration. The weakness of this correlation, however, indicates that the hydrodynamic sorting signal is substantially overprinted by anthropogenic modifications, particularly the construction of protective structures that disrupt natural sediment transport pathways and introduce localised depositional anomalies decoupled from the prevailing erosion-accretion dynamics.

The near-negligible correlation between shoreline change rate and mean grain size (R = 0.15) (Fig. 15) confirms that grain size is effectively independent of shoreline change intensity along this coastline, and that textural variability alone cannot serve as a reliable proxy for erosion or accretion behaviour in structurally modified littoral environments. The moderate negative relationship between mean grain size and HM concentration (R = -0.55) (Fig. 15) reflects the mutual dependence of these two variables on hydrodynamic sorting processes, whereby finer sediments tend to concentrate heavier minerals under the selective transport action of waves and longshore currents, a pattern consistent with findings reported for the broader Nile Delta coast (Frihy and Komar, 1993; Frihy and Dewidar, 2003). Importantly, this relationship is governed not solely by hydrodynamic factors but also by human intervention, as evidenced by the structural anomalies at sites A1 and A9.

These findings are broadly consistent with those reported for the Nile Delta coast, where seabed change rates were consistent with heavy mineral distribution but not with mean grain size (Frihy and Komar, 1993; Frihy and Dewidar, 2003). In the present study, however, the nodal points confining the littoral sub-cell boundaries have been largely modified, resulting in varied erosion and accretion patterns. This modification is primarily attributed to the construction of coastal protective structures, which have disrupted the continuity of sediment transport and prevented Nile-sourced sediments from entering the littoral drift system. Consequently, care must be taken when employing textural and mineralogical trends to determine coast-wide patterns of net sediment transport in anthropogenically modified coastal systems.

CONCLUSIONS

This study presents a comprehensive multi-temporal shoreline change analysis along the Rosetta coastline over two periods, 1999–2019 and 1999–2015, integrated with sediment textural and heavy mineral characterisation, to provide a coupled morphodynamic and sedimentological assessment of one of the most erosion-vulnerable sectors of the Nile Delta coast. Shoreline change analyses for the entire study period (1999–2019) revealed a dominant erosional regime, with a mean shoreline change rate of -3.65 m/year. The mean erosion rate was estimated at 7.92 m/year across the study area, affecting approximately 70% of the total coastline length (~22 km), and reflecting the severity of retreat along the eroded fraction of the coastline. The western sector sustained severe and spatially extensive land loss, with a mean shoreline change of -6.09 m/y and erosion affecting ~95% of its length, driven primarily by the chronic depletion of Nile-derived sediment discharge following upstream dam construction and the interception of westward longshore flux by the western seawall.

The coastal sector of B exhibited three complex erosion-sediment transport-accretion cycling patterns, with a mean shoreline change of -3.4 m/year and an extreme erosion rate of 32.51 m/year recorded downdrift of the fifth eastern groin, the highest value quantified along the entire study area, reflecting the compounding effects of seawall/groyne-field infrastructure on sediment transport discontinuity and localised erosion acceleration. The easternmost sector remained the least dynamically active, recording a mean change of -1.11 m/year. Despite that, its complete dominance of erosion and absence of meaningful sediment supply render it inherently vulnerable to progressive long-term erosion.

The comparative analysis of the 1999–2015 and 1999–2019 study periods revealed an important temporal evolution in coastal dynamics. While the spatial extent of erosion expanded over the full study period, the mean erosion rate (-8.65 m/year) and peak erosion value (35.87 m/year) recorded during 1999–2015 exceeded their 1999–2019 equivalents, attributable to the partial sediment-retaining effect of the Ghalioun fish farm, constructed after 2015. This finding underscores the capacity of localised engineering interventions to partially redistribute, though not reverse, the erosional signal within a chronically sediment-starved littoral system.

Shoreline projections for 2030, derived from the 1999–2019 LRR rates, indicated a mean coastline recession of 108 m and a net land loss of 2.24 km² in the absence of coastal management intervention, partially offset by a projected accretion gain of 0.74 km² concentrated in the eastern sector. These projections represent a conservative minimum-bound estimate, as the anticipated full operational sediment retention by the Grand Ethiopian Renaissance Dam (GERD) is expected to further deplete the already deficient Nile Delta littoral sediment budget beyond the rates captured in the historical record, rendering actual shoreline recession by 2030 potentially more severe than modelled.

The sedimentological analysis revealed a fine-sand-dominated littoral environment (mean grain size 2.42 Φ) overlain by density lags of heavy mineral concentrates, with total HM concentrations ranging from 0.71 to 23.14 wt.% and a mean of 10.21 wt.%. The spatial distribution of HM enrichment is strongly controlled by proximity to the Rosetta promontory, which functions as the principal source of heavy mineral-enriched Nile-derived sediments to the littoral system, with concentrations diminishing progressively with distance from the source in both longshore directions. The majority of sampled locations exceed the 2 wt.% economic viability threshold, confirming the presence of promising beach placer deposits along the Rosetta coastline with potential for local industrial exploitation and exportation. The weak negative correlation between HM concentration and shoreline change rate (R = -0.37) is consistent with lag concentration processes in erosional settings. The near-negligible correlation between grain size and shoreline change rate (R = 0.15) confirms that textural variability is not a primary control on erosion-accretion processes. The moderate negative relationship between grain size and HM concentration (R = -0.55) reflects hydrodynamic sorting under dominant eastward longshore transport. This signal is substantially modified by anthropogenic interference from coastal protective structures, which have disrupted the natural continuity of sediment transport and altered the expected mineralogical and textural distribution patterns.

Collectively, these findings demonstrate that shoreline change along the Rosetta coastline is governed by a hierarchical interplay of regional sediment starvation driven by Nile impoundment that established the background erosional trend, and coastal engineering infrastructure that redistributed and locally amplified this signal, producing a spatially complex mosaic of erosion, sediment transport and accretion that is further reflected in the sediment mineralogical and textural record. The Nile Delta has already been identified as highly vulnerable to accelerating sea-level rise and continued upstream sediment impoundment under future climate change scenarios. These results highlight the urgent need for integrated coastal management strategies, including beach nourishment, structural reconfiguration, and long-term monitoring of sediment budget, to mitigate the projected acceleration of land loss and safeguard the long-term stability of the Rosetta coastline and the communities and infrastructure it supports.

REFERENCES

Anil Cherian, N., Chandrasekar, G., Rajamanickam, V., Gujar, A.R., 2011. An evaluation of major placer minerals along the Valinokkam–Tuticorin Coast, Southern Tamil Nadu, India. International Journal of Earth Sciences and Engineering 4, 1031–1035.

Becker, R.H., Sultan, M., 2009. Land subsidence in the Nile Delta: Inferences from radar interferometry. The Holocene 19(6), 949–954.

Behera, P., 2003. Heavy minerals in beach sands of Gopalpur and Paradeep along Orissa coastline, east coast of India. Indian Journal of Marine Sciences 32, 172–174.

Coleman, J.M., Robert, H.H., Murray, S.P., Salama, M., 1981. Morphology and dynamic sedimentology of the eastern Nile delta shelf. Marine Geology 42, 301–312.

Dolan, R., Hayden, B.P., May, S., 1983. Erosion of the US shorelines. In: Komar, P.D. (Ed.), CRC handbook of coastal processes and erosion. Boca Raton, Florida: CRC Press, 285–299.

Dolan, R., Fenster, M.S., Holme, S.J., 1991. Temporal analysis of shoreline recession and accretion. Journal of Coastal Research 7(3), 723–744.

Douglas, B.C., Crowell, M., 2000. Long-term shoreline position prediction and error propagation. Journal of Coastal Research 16(1), 145–152.

Elsherif, E.A., Badawi, A., Abdelkader, T., 2020. Grain size distribution and environmental implications of Rosetta beach, Mediterranean Sea coast, Egypt. Egyptian Journal of Aquatic Biology and Fisheries 24(1), 349–370.

El Banna, M.M., Frihy, O.E., 2009. Human-induced changes in the geomorphology of the northeastern coast of the Nile delta, Egypt. Geomorphology 107, 72–78.

El Wany, M.H., Khafagy, A.A., Inman, D.L., Fanos, A.M., 1988. Analysis of waves from arrays at Abu Quir and Ras El Bar, Egypt. Advances in Underwater Technology, Ocean Science and Offshore Engineering 16, 89–97.

El-Asmar, H.M., Hereher, M.E., 2010. Change detection of the coastal zone east of the Nile Delta using remote sensing. Environmental Earth Sciences 62, 769–777.

Fanos, A.M., Naffaa, M.G., Fouad, E.E., Omar, W., 1995. Seasonally and yearly wave regime and climate of the Mediterranean coast of Egypt. Fourth International Conference on Coastal and Port Engineering in Developing Countries, Rio de Janeiro, Brazil, pp. 2075–2093.

Fenster, M., Dolan, R., Elder, J., 1993. New method for predicting shoreline positions from historical data. Journal of Coastal Research 9, 147–171.

Frihy, O.E., 2017. Evaluation of future land-use planning initiatives to shoreline stability of Egypt's northern Nile delta. Arabian Journal of Geosciences 10(5), 109.

Frihy, O.E., Dewidar, K.M., 2003. Patterns of erosion/sedimentation, heavy mineral concentration and grain size to interpret boundaries of littoral sub-cells of the Nile Delta, Egypt. Marine Geology 199(1–2), 27–43.

Frihy, O.E., Khafagy, A.A., 1991. Climate and induced changes in relation to shoreline migration trends at the Nile Delta promontories, Egypt. Catena 18(2), 197–211.

Frihy, O.E., Komar, P.D., 1991. Patterns of beach-sand sorting and shoreline erosion on the Nile Delta. Journal of Sedimentary Petrology 61, 544–550.

Frihy, O.E., Komar, P.D., 1993. Long-term shoreline changes and the concentration of heavy minerals in beach sands of the Nile Delta, Egypt. Marine Geology 115, 253–261.

Frihy, O.E., Lawrence, D., 2004. Evolution of the modern Nile Delta promontories: Development of accretional features during shoreline retreat. Environmental Geology 46, 914–931.

Frihy, O.E., Lotfy, M.F., 1994. Mineralogy and texture of beach sands in relation to erosion and accretion along the Rosetta Promontory of the Nile Delta, Egypt. Journal of Coastal Research 10, 588–599.

Frihy, O.E., Lotfy, M.F., 1997. Shoreline changes and beach-sand sorting along the northern Sinai coast of Egypt. Geo-Marine Letters 17, 140–146.

Frihy, O.E., Fanos, A.M., Khafagy, A.A., Komar, P.D., 1991. Patterns of nearshore sediment transport along the Nile Delta, Egypt. Coastal Engineering 15(5–6), 409–429.

Frihy, O.E., Debes, E., El Sayed, W., 2003. Processes reshaping the Nile Delta promontories of Egypt: Pre- and post-protection. Journal of Geomorphology 53, 263–279.

Frihy, O.E., Shereet, S., El Banna, M., 2008. Pattern of beach erosion and scour depth along the Rosetta promontory and their effect on the existing protection works, Nile Delta, Egypt. Journal of Coastal Research 24, 857–866.

Frihy, O.E., Deabes, E., Shereet, S., Abdalla, F., 2010. Alexandria-Nile Delta coast, Egypt: Update and future projection of relative sea-level rise. Environmental Earth Sciences 61, 253–273.

Ghoneim, E., 2009. A remote sensing study of some impacts of global warming on the Arab Region. In: Tolba, M., Saab, N. (Eds.), Report on Arab Environment, Climate Change: The Arab Forum for Environment and Development (AFED), Beirut, pp. 31–46.

Ghoneim, E., Mashaly, J., Gamble, D., Halls, J., AbuBakr, M., 2015. Nile Delta exhibited a spatial reversal in the rates of shoreline retreat on the Rosetta promontory comparing pre-and post-beach protection. Geomorphology 228, 1–14.

Hereher, M.E., 2010. Vulnerability of the Nile Delta to sea level rise: an assessment using remote sensing. Geomatics, Natural Hazards and Risk 1(4), 315–321.

Hereher, M., 2011. Mapping coastal erosion at the Nile Delta western promontory using Landsat imagery. Environmental Earth Sciences 64, 1117–1125.

Hilmy, M.E., 1951. Beach sands of the Mediterranean coast of Egypt. Journal of Sedimentary Research 21, 109–120.

Inman, D.L., Brush, B.M., 1973. The coastal challenge. Science 181 (4094), 20–32.

Inman, D.L., Jenkins, S.A., 1984. The Nile littoral cell and man's impact on the coastal zone of the southeastern Mediterranean. Proceedings of 19th International Conference on Coastal Engineering, American Society of Civil Engineers, 1600–1617.

Iskander, M., 2010. Environmental friendly methods for the Egyptian coastal protection. In: First international conference on Coastal Zone Management of River Deltas and Low Land Coastlines 1(32), 625–642.

Kevin, W., El Asmar, H.M., 1999. Monitoring changing position of coastline using Thematic Mapper Imagery, an example from the Nile Delta. Geomorphology 29(1–2), 93–105.

Komar, P.D., 1998. Beach processes and sedimentation. Upper Saddle River, New Jersey: Prentice Hall Inc., 544 p.

Landsat Project Science Office, 2008. The Landsat-7 science data user's handbook. Goddard Space Flight Center, NASA, Greenbelt, MD, USA, 186 p.

Li, R., Di, K., Ma, R., 2001. A comparative study of shoreline mapping techniques. The Fourth International Symposium on Computer Mapping and GIS for Coastal Zone Management, Halifax, Nova Scotia, Canada, 53–60.

Manohar, M., 1976. Beach profiles. Proceedings of UNESCO Seminar on Nile Delta Sedimentology, Alexandria, 95–99.

Manohar, M., 1981. Coastal processes along the Nile Delta coast, shore and beach. Journal of Coastal Research 49, 8–15.

Marriner, N., Flaux, C., Morhange, C., Kaniewski, D., 2012. Nile Delta's sinking past: Quantifiable links with Holocene compaction and climate-driven changes in sediment supply? Geology 40(12), 1083–1086.

Milner, H.B., Ward, A., Hingham, F., 1962. Sedimentary Petrography, 4th Rev.

Moore, L.J., 2000. Shoreline mapping techniques. Journal of Coastal Research 16(1), 111–124.

Nafaa, M.G., Frihy, O.E., 1993. Beach and nearshore features along the dissipative coastline of the Nile Delta, Egypt. Journal of Coastal Researc, 9 (2), 423–433.

Orlova, G., Zenkovich, V., 1974. Erosion of the shores of the Nile Delta. Geoforum 5, 68–72.

Pupienis, D., Buynevich, I.V., Bitinas, A., 2011. Distribution and significance of heavy-mineral concentrations along the southeast Baltic Sea coast. Journal of Coastal Research 64, 1984–1988.

Raju, P.D.R., Neelima, G., 2012. Image segmentation by using histogram thresholding. International Journal of Computer Science Engineering and Technology 2(1), 776–779.

Ravindra Kumar, G.R., Sreejith, C., 2010. Relationship between heavy mineral placer deposits and hinterland rocks of southern Kerala: A new approach for source-to-sink link from the chemistry of garnets. Journal of Geo-Marine Sciences 39, 562–571.

Shalash, S., 1982. Sedimentation in the Aswan High Dam Reservoir. Hydrobiologia 92, 623–629.

Smith, S., Abdel-Kader, A., 1988. Coastal erosion along the Egyptian Delta. Journal of Coastal Research 4, 245–255.

Stanley, D.J., Warne, A.G., 1993. Nile Delta: recent geological evolution and human impact. Science 260(5108), 628–634.

Stanley, D.J., 1988. Subsidence in the northern Nile Delta: Rapid rates, possible causes and consequences. Science 240, 497–500.

Stanley, D.J., Corwin, K., 2013. Measuring strata thicknesses in cores to assess recent sediment compaction and subsidence of Egypt's Nile delta coastal margin. Journal of Coastal Research 29, 657–670.

Thieler, E.R., Himmelstoss, E.A., Zichichi, J.L., Ergul, A., 2009. Digital Shoreline Analysis System (DSAS) version 4.0—An ArcGIS extension for calculating shoreline change, U.S. Geological Survey, Open-File Report, 2008–1278.

UNESCO/UNDP, 1978. Coastal protection studies of the Nile Delta. Final Technical Report, Paris, 1, 155 p.

Van Rijn, L.C., 2011. Coastal erosion and control. Ocean & Coastal Management 54(12), 867–887.

Wassef, S.N., 1973. Distribution of monazite in the black sands of Rosetta and Damietta and its condition of sedimentation. Ph.D. Thesis, Faculty of Science, Ain Shams University, Cairo, Egypt.

White, K., El-Asmar, H., 1999. Monitoring changing position of coastlines using Thematic Mapper imagery, an example from the Nile Delta. Geomorphology 29, 93–105.

Woolsey, J.R., Henry, V.J., Hunt, J.L., 1975. Back shore heavy mineral concentration on Sapelo Island, Georgia. Journal of Sedimentary Petrology Research 45, 280–284.